

FIRST DETECTION OF PAHS AND WARM MOLECULAR HYDROGEN IN TIDAL DWARF GALAXIES

S. J. U. HIGDON¹ J. L. HIGDON¹ & J. MARSHALL¹

Draft version October 26, 2018

ABSTRACT

We observed two faint tidal dwarf galaxies (TDGs), NGC 5291 N and NGC 5291 S with the Infrared Spectrograph on the Spitzer Space Telescope. We detect strong polycyclic aromatic hydrocarbon (PAH) emission at 6.2, 7.7, 8.6, 11.3, 12.6 and 16.5 μm , which match models of groups of ~ 100 carbon atoms with an equal mixture of neutral and ionized PAHs. The TDGs have a dominant warm ~ 140 K dust component in marked contrast to the cooler, 40 – 60 K dust found in starburst galaxies. For the first time we detect the low-J rotational lines from molecular hydrogen. Adopting LTE there is $\sim 10^5 M_{\odot}$ of ~ 400 K gas, which is $< 0.1\%$ of the cold gas mass inferred from ^{12}CO (1-0) measurements. The combination of one-third solar metallicity with a recent, < 5 million year, episode of star formation is reflected in the S and Ne ratios. The excitation is higher than typical values for starburst galaxies and similar to that found in BCDs. Using the Infrared Array Camera we identify an additional 13 PAH-rich candidate TDGs. These sources occupy a distinct region of IRAC color space with $[3.6] - [4.5] < 0.4$ and $[4.5] - [8.0] > 3.2$. Their disturbed morphologies suggest past merger events between companions, for example, NGC 5291 S has a projected 11 kpc tail. NGC 5291 N and S have stellar masses of $(1.5 \text{ and } 3.0) \times 10^8 M_{\odot}$, which is comparable to BCDs, though still roughly 10% of the LMC's stellar mass. The candidate TDGs are an order of magnitude less massive. This system appears to be a remarkable TDG nursery.

Subject headings: galaxies: dwarf — galaxies: interactions — individual (NGC 5291, NGC 5291 S, NGC 5291 N) — galaxies: formation — infrared: galaxies

1. INTRODUCTION

In addition to triggering starbursts and active galactic nuclei, mergers of dusty, gas rich disk galaxies frequently lead to the formation of tidal tails stretching $\gtrsim 100$ kpc from the site of the collision (Toomre & Toomre 1972; Schweizer 1978; Sanders & Mirabel 1996). These structures tend to be HI rich with blue optical colors, reflecting both their origin in the outer spiral disk and on-going star formation (van der Hulst 1979; Schombert Wallin & Struck-Marcell 1990, Mirabel, Lutz & Mazza 1991; Hibbard & van Gorkom 1996). Zwicky (1956) proposed that dwarf galaxies might form out of self-gravitating clumps within tidal tails, and indeed, concentrations of gas and star forming regions, with dwarf galaxy size HI masses and optical luminosities, are commonly found. Computer simulations of merging galaxies typically give timescales of $\sim 10^8$ years for the formation of condensations at the tips of the ~ 100 kpc tails, indicating that any young stellar population has been formed in-situ and has not simply been stripped from the host galaxy disk.

The cataloging of Tidal Dwarf Galaxies (TDGs) is still in its infancy. Kinematic observations alleviate potential contamination from foreground and background objects. However projection effects can give the appearance of a bound object to unbound condensations in the debris left over from galaxy interactions. A bona fide TDG should be self-gravitating, rotating, long-lived and tidal in origin. Tidal origin and longevity can only be inferred from comparison of the source morphology and kinematics with simulations. It is often impossible to fully disentangle tidal effects from other dynamical effects such as ram pressure stripping. Whether or not most candidate

TDGs are subject to tidal disruption and re-absorption by the merger remnant on $\sim \text{Gyr}$ timescales is still an open question (e.g., Hibbard & Mihos 1995; Elmegreen, Kaufman & Thomasson 1993). The formation of both TDGs and transient unbound star-forming regions will enrich the outer regions of the inter-galaxy medium.

The study of dwarf irregular proto/young galaxies formed either via tidal interactions between the parent galaxies or from ram-sweeping of debris material, and collectively called TDGs, may be an important part of galaxy formation and evolution. TDGs located at the tips of optically faint but HI rich tails represent new star forming systems largely free of pre-existing stellar populations, and represent useful templates of star formation in the early universe, albeit with higher metallicity (Duc & Mirabel 1998, hereafter, DM98). More importantly, dwarf galaxies are by far the most common galaxy type in the current epoch, accounting for 38 out of 41 galaxies in the Local Group alone (Mateo 1998). Work by Hunsberger et al. (1996) suggests that TDGs may make up at least 1/3 and possibly 1/2 of the dwarf galaxy population in compact groups i.e., a potentially significant galaxy formation mechanism in the current epoch. One problem with this scenario is dark matter. Like massive spirals, dwarf galaxies appear to be dominated by dark matter. If dark matter is non-baryonic it is hard to form a halo around a dwarf galaxy that has been formed via tidal interaction. If the dark matter is baryonic i.e., cold molecular gas (Pfenniger, Combes & Martinet 1994) then the TDG/dwarf association remains a valid possibility. Both the nature of dark matter and whether the dynamical masses of TDGs infers its presence are still open questions.

Studies of TDG properties may help us better understand the dwarf galaxy population as a whole, such as

¹ Astronomy Department, Cornell University, Ithaca, NY 14853

what fraction are truly primordial building blocks of massive galaxies left over from the epoch of galaxy formation, and what fraction may be TDGs from high and intermediate red-shifts. This is especially relevant as the merger rate was likely much higher at $z > 1$ than it is today. To date the TDG sample is still too small to statistically assess the importance of this population of objects. That assessment will be made in due course. Whether rare or ubiquitous, these objects warrant detailed study. Here we utilize the unique capabilities of the Spitzer Space Telescope (Werner et al. 2004a) to study the NGC 5291 system, which is known for its remarkably rich proto/young galaxy nursery.

NGC 5291 is a disturbed elliptical/lenticular galaxy located at the western edge of the cluster Abell 3574. Pedersen et al. (1978) briefly discussed deep images of the system taken with the ESO 3.6 m telescope. They highlighted the presence of many optical knots, which they suggested were extragalactic HII regions. Longmore et al. 1979 (hereafter, L79) published a much more detailed investigation. Using deep Schmidt plates with filters approximating B ($\Delta\lambda$ 3950 - 5400 Å Schott GG395 filter/III-aJ emulsion) and U ($\Delta\lambda$ 3200 - 3900 Å Schott UG1 filter/III-aJ emulsion) passbands they found 24 blue knots extending across an arc centered on NGC 5291 and obtained spectra of the eight brightest. They identified the knots as giant extragalactic HII regions, but noted that both the projected linear size and optical luminosity of the largest knots were greater than the Large Magellanic Cloud. Coincidentally, Maza et al. (1991) also obtained spectra of the brightest optical knot, which was included in an object prism survey of HII galaxies. Using the Parkes radio telescope, L79 also discovered a large HI mass ($\sim 10^{11} M_{\odot}$) associated with NGC 5291 and its blue knots though slightly displaced to the west. Malphrus et al. (1997, hereafter, M97) mapped the HI 21 cm emission using the VLA. The HI morphology resembles a large fragmented ring with a continuous eastern arc stretching ~ 4 arcmin (72 kpc) on either side of NGC 5291. The eastern half of the ring contains most of the neutral hydrogen as well as the highest HI surface densities, and is associated with both NGC 5291 and its knots of star formation. The origin of this giant HI ring is still unclear. NGC 5291 has a disturbed companion galaxy called the “Seashell”, however it is unlikely that this galaxy is linked to the HI ring’s formation as it is both gas poor and has a much higher radial velocity ($\sim 600 \text{ km s}^{-1}$) relative to NGC 5291, indicating a high fly-by velocity (L79, $> 400 \text{ km s}^{-1}$, DM98). L79 discussed several models for the origin of NGC 5291. They noted that the optical morphology is similar to the Antennae (NGC 4038/39) and that there are two other galaxies (# 435 and 446 in Richter 1984) within 150 kpc projected distance from NGC 5291 that may be responsible for a tidal interaction. However M97 rule out the interplay for both galaxies. They detected Richter 435, which lies $\sim 4'$ southwest of NGC 5291, in HI, but with a heliocentric velocity $\sim 250 \text{ km s}^{-1}$ lower than the HI ring. M97 found that, like the Seashell, there is little HI associated with the second candidate galaxy Richter 446, $\sim 5'$ northeast of NGC 5291. However, L79’s preferred model for the system is that a pre-existing giant HI disc has undergone compression and possible ram pressure

sweeping by the intra-cluster medium as the system falls into the cluster from the far side. L79 suggested that the knots could eventually form a population of blue dwarf irregular galaxies. The combined optical and VLA observations led M97 to revive the tidal model and they conclude that the system is probably both interacting and likely being ram-swept as it moves through the intra-cluster medium.

However mysterious its origin the NGC 5291 system is a remarkable galactic nursery. M97 investigated whether the knots are self-gravitating and will remain bound against the tidal force of the parent galaxy to become dwarf irregular galaxies. They compared the HI mass for each knot to the binding mass. They argued that for the two most massive HI clumps, NGC 5291 N (hereafter, TDG-N), and NGC 5291 S (hereafter, TDG-S) the combined mass of stars and gas will result in self-gravitating knots. M97 also calculated the radius at which material in a knot would be disrupted by the tidal force with the parent galaxy and compared it to the projected radius of the HI knots. The majority of the knots, including TDG-N and TDG-S, appear to be tidally stable. Using H α Fabry-Perot observations Borunaud et al. (2004) were able to determine the rotation curve for TDG-N, clearly showing that it is self-gravitating and rotating. They concluded that higher resolution observations are required to assess the presence of dark matter.

Before the launch of the Spitzer Space Telescope, mid-infrared spectroscopic studies of objects as faint as TDGs were not feasible. We have taken advantage of the unprecedented sensitivity of the Spitzer Space Telescope to obtain IRS spectra of the two optically brightest TDGs in the NGC 5291 system, TDG-N and TDG-S at the northern and southern-most tips of the high surface density HI arc. The mid-infrared region of the spectrum is rich in atomic and molecular emission features from the star forming ISM, including fine structure lines like [Ne II], polycyclic aromatic hydrocarbons (PAHs) and warm molecular hydrogen. This will allow comparisons with similar mid-infrared studies of other star forming galaxies from dwarf irregulars to massive spirals.

We have also imaged the eastern half of the HI ring, including the associated proto/young irregular galaxy population, NGC 5291 and the “Seashell”, with the Infrared Array Camera (Fazio et al. 2004, IRAC). We assess the relative contributions from both cool (evolved and low mass main sequence) stars and from star formation as traced by PAH emission in the $8.0 \mu\text{m}$ band. The resulting mid-infrared spectral energy distribution (SED) and colors will allow useful comparisons with other galaxy types.

In §2 we detail the observations and data reduction. §3 begins with the results and discussion of the the mid-infrared spectral properties of TDG-N & TDG-S. We compare the stellar and non-stellar (i.e., PAH) morphology of NGC 5291, the “Seashell”, and the knots next in §§3.2 – 3.4. In §3.5 we select a population of candidate TDGs by matching the IRAC SEDs to galaxy templates. We investigate the mid-infrared color-color and color-magnitude relations in §3.6. We estimate the TDG stellar masses in §3.7 and present our conclusions in §4. We adopt a luminosity distance of 62 Mpc to the NGC 5291 system. This distance is calculated using the red-shift in NED with $H_0 = 71 \text{ km s}^{-1} \text{ Mpc}^{-1}$, $\Omega_M =$

0.27, $\Omega_\Lambda = 0.73$. & $\Omega_k = 0$, and does not reflect any uncertainty in the distance due to proper motion within the group. This gives a linear scale of $1'' = 0.3$ kpc.

2. OBSERVATIONS & DATA REDUCTION

2.1. IRS Spectroscopy

IRS observations were taken of both TDG-N and TDG-S. The IRS low resolution data were obtained with Short-low (IRS-SL), which operates between 5.2 and 7.7 μm (IRS-SL2) and 7.4 - 14.5 μm (IRS-SL1). IRS-SL has a resolving power of $64 \leq \frac{\lambda}{\Delta\lambda} \leq 128$. The high resolution data were obtained using Short-high (IRS-SH), which encompasses the range 9.9 - 19.6 μm , and Long-high (IRS-LH), which spans 18.7 - 37.2 μm . The two high resolution spectrometers have a resolving power, $\frac{\lambda}{\Delta\lambda} \sim 600$.

Observations were made in the IRS Staring Mode AOR with a high accuracy blue peak-up using a star from the 2MASS catalogue (Cutri et al. 2003). The staring mode AOR integrated for half the time listed in Table 1 at each of the two nominal nod positions on each slit. The spectral data were processed as far as the un-flat-fielded two dimensional image using the standard IRS S11 pipeline. See chapter 7 of the Spitzer Observers Manual (SOM)² for further observing mode and pipeline details.

Both TDG-N and TDG-S have extended emission at 8 μm with respect to the IRS slits (3.6'' IRS-SL, 4.7'' IRS-SH and 11.1'' IRS-LH). The spectra were extracted and sky subtracted using the extended source routines in the SMART analysis package (Higdon et al. 2004). The IRS-SH and IRS-LH data were extracted using the full aperture and the IRS-SL spectra were extracted using a column of 20'' fixed width. The spectra were flat-fielded and flux-calibrated by extracting and sky subtracting un-flat-fielded observations of the calibration stars HR 6348 (IRS-SL) and ksi Dra (IRS-SH, IRS-LH), and dividing these data by the corresponding template (Cohen 2003) to generate a 1-dimensional relative spectral response function (RSRF). The RSRF was then applied to the TARGET observations to produce the final spectra. The residual sky was subtracted from the IRS-SL data using the off-source observations, which are part of the Staring mode AOR. A Zodiacal light model from the Spitzer Planning Observations Tool (SPOT) was scaled to the IRS slits and subtracted from the IRS-SH and IRS-LH data. An aperture correction of 0.85 was applied to the IRS-SL spectra as the sources are extended. In addition, the IRS-LH TDG-N and TDG-S spectra were scaled by 0.30 and 0.26, respectively in order to stitch to the IRS-SH spectra. The scale factors are close to the simple geometric aperture correction for the differing IRS-SH and IRS-LH slits which is 0.215. However, these sources are not uniformly extended and the two apertures are orientated $\sim 85^\circ$ with respect to each other.

2.2. IRAC Imaging

IRAC data in all four bands were acquired using a two point map centered on NGC 5291 ($\alpha_{J2000} = 13^{\text{h}}47^{\text{m}}23.00^{\text{s}}$, $\delta_{J2000} = -30^\circ25'30.0''$). The array was aligned to celestial north and stepped by 180''. Three 3 s frames were taken in each channel using a 12 position Reuleaux dither pattern with a medium scale fac-

tor, resulting in a total integration time of 432 s. Due to the footprint of the IRAC arrays the resulting map has a total area of 110.8 arcmin² with a sub-region of 59.1 arcmin² sampled by all 4 channels. In this paper we will only discuss the properties of sources located in this sub-region. The IRAC data were processed through version S11.0.2 of the SSC-IRAC pipeline. For more observing mode and pipeline information see chapter 6 of the SOM.

The IRAC was designed to map both interstellar emission and starlight. The 3.6 & 4.5 μm bands primarily trace the stellar mass distribution, as the emission at these wavelengths is well approximated by the Rayleigh-Jeans limit of blackbody emission for both early- and late-type stars. At 8 μm the mid-IR traces dust emission, in particular the 7.7 & 8.6 μm PAH features from the interstellar medium. It is straight forward to subtract the stellar emission from the 8 μm image to produce the PAH/dust image shown in Figure 1. The method is outlined in Pahre et al. (2004). The 3.6 and 4.5 μm images are scaled to match the theoretical colors of MO III stars ([3.6] - [4.5] = -0.15, [4.5] - [5.8] = +0.11 and [5.8] - [8.0] = +0.04) at 8 μm , and subtracted from the 8 μm image.

SExtractor (Bertin & Arnouts 1996) was used to generate a catalog of sources for each IRAC channel. We then selected all sources that were identified in all four channels with a positional uncertainty of $\leq 2''$. SExtractor was also run on the dust image to find an additional 14 sources which were not detected in all four channels. For these sources SExtractor was re-run on the 3.6 through 8.0 μm images using the source positions determined from the 8 μm image. Table 4 lists the flux densities in an 8 pixel (9.8'') diameter aperture. A 16 pixel (19.5'') diameter aperture was used for a few sources, including TDG-N and TDG-S. The flux densities were corrected to a 20 pixel radius aperture using the following scale factors 1.086 & 1.017 (3.6 μm), 1.098 & 1.018 (4.5 μm), 1.097 & 1.020 (5.8 μm) and 1.118 & 1.026 (8.0 μm) for the 8 and 16 pixel apertures respectively, as determined by the IRAC team. The auto-flux returned from SExtractor is included for objects that are extended beyond the 19.5'' circular aperture, such as NGC 5291 and the Seashell. The Vega zero magnitude flux densities in the four IRAC bands are 277.5, 179.5, 116.6 and 63.1 Jy at 3.6, 4.5, 5.8 and 8.0 μm respectively. Stellar sources were removed from the catalog if they matched one of the following criteria: 2MASS (J - K) ≤ 0.5 (Eisenhardt 2004), identified as stellar sources in the Hubble Guide Star Catalogue Version 2.2, or through visual inspection of the IRAC images.

3. RESULTS AND DISCUSSION

3.1. Mid-Infrared Spectral Properties of TDG-N & TDG-S

The top of Figures 2 & 3 show the IRS-SL spectra of TDG-N and TDG-S. The broad emission features from PAHs at 6.2, 7.7, 8.6 and 11.3 μm are clearly present. Bright fine structure lines of [S IV] 10.51 μm and [Ne II] 12.81 μm emission lines are also apparent in this low resolution spectrum, as is a weak rotational 0-0 S(3) 9.66 μm line from molecular hydrogen. Figure 4 shows the IRS-SL spectrum of TDG-N overlaid with the IRS-SL spectrum of the reflection nebulae NGC 7023 (Werner et al. 2004b) and the ISO-SWS spectrum of M 82's nucleus (Lutz et al. 1998), smoothed to the IRS-SL reso-

² <http://ssc.spitzer.caltech.edu/documents/som/>

lution. The overlay spectra are normalized to TDG-N's flux density at $7 \mu\text{m}$. Here we are using NGC 7023 to characterize a low ionization star forming region as it is illuminated by HD 200775, a B2Ve star. M 82 is used to represent the mid-infrared spectrum of a starburst. The three spectra are remarkably similar in shape and only a detailed analysis will reveal their differing environments. To assess whether the PAHs in TDG-N and TDG-S are similar to those in M 82 we fit the continuum emission in the IRS-SL spectrum with the thermal radiation from a distribution of graphite and silicate grains and the PAHs with a series of Drude profiles. Table 2 lists the resulting PAH fluxes and equivalent widths. The relative strength of the $11.3/7.7 \mu\text{m}$ PAHs in TGN-N (TDG-S) is 0.22 ± 0.03 (0.23 ± 0.05) and $6.2/7.7 \mu\text{m}$ PAHs 0.35 ± 0.06 (0.33 ± 0.11). These values are consistent with groups of ~ 100 carbon atoms in an approximately equal mixture of neutral and ionized PAHs (see Figure 16 in Draine & Li 2001). For comparison, on the same Figure, the PAH ion fraction is close to unity in M 82 with similar sized clumps of C atoms. In addition to the PAH features observed in the IRS-SL spectra, we also detect PAH emission at 13.5 and $16.5 \mu\text{m}$ in the IRS-SH spectra, the $16.5/7.7 \mu\text{m}$ PAH ratio is 0.02 ± 0.01 and 0.10 ± 0.05 in TDG-N and TDG-S.

Figures 2, bottom & 3, bottom show the IRS-SH & IRS-LH spectra. The fine structure neon and sulfur lines are prominent as well as weak 0-0 S(1) and 0-0 S(2) emission from H_2 . The spectra flatten out around $\lambda > 20 \mu\text{m}$. A similar flattening is seen in the extremely low metallicity blue compact dwarf galaxy SBS0335-052 (Houck et al. 2004b). Using SMART we fit a diluted black-body to the continuum over the range $15 - 35 \mu\text{m}$. Using a solid angle equal to the IRS-SH aperture of 1.35×10^{-10} sr gives a temperature $T = 139 \pm 6$ K. The derived optical depth at $0.55 \mu\text{m}$ ($\tau_{0.55\mu\text{m}}$) is effectively zero, and $\alpha = 1.2 \pm 0.2$ where, $\tau = \tau_{0.55\mu\text{m}}(0.55/\lambda)^\alpha$. A similar result is obtained for TDG-S with a temperature $T = 142 \pm 31$ K. A dominant cooler $40 - 60$ K dust component that is present in most starbursts and spiral galaxies is absent.

Figures 5 & 6 show the line profiles from the IRS observations. The line fluxes and equivalent widths for both TDGs are given in Table 3. No correction has been made for reddening as the optically derived extinction is low, typically, $A_B \leq 1$ mag. (L79, Pena, Ruiz & Maza 1991, DM98). Geometric effects can also make any extrapolation from the optical to the infrared highly uncertain. In the following paragraphs we use the line strengths and ratios to derive physical properties of the ionized and molecular ISM in the TDGs.

Both the Ne and the S line ratios can be used to constrain the properties of the underlying starburst. The starburst sample of Thornley et al. (2000) have typical $[\text{Ne III}]/[\text{Ne II}]$ ratios between 0.05 and 1.0. For example, M 82 has a neon ratio of 0.18. The exceptions to this range are the two low metallicity dwarf galaxies, NGC 5253 and II Zw 40, which both have one-fifth solar metallicity. These have neon ratios of 3.5 and 12, respectively. Lowering the metallicity produces "hotter" main sequence stars for a given mass, and the radiation is harder due to reduced line blanketing and blocking, hence the neon ratio increases. The TDG-N and TDG-S have neon ratios of 2.4 ± 0.1 and 1.4 ± 0.1 respectively,

which is consistent with their one-third solar metallicity (L79, Pena, Ruiz & Maza 1991, DM98). Figure 10 from Thornley et al. (2000) gives an age for the most recent episode of star formation of ~ 5 million years for these neon ratios for a galaxy with one-fifth solar metallicity and $\log U = -2.3$, where U is the number of ionizing photons at the surface of the nebula per hydrogen atom. This result is consistent with the starburst age derived from optical spectra by DM98. Both TDG-N and TDG-S have slightly higher metallicity, as well as fewer ionizing photons (i.e., $\log U = -3$), as inferred from model excitation diagrams in Pena, Ruiz & Maza (1991, for TDG-S we used emission lines from DM98). Both these effects will result in a younger burst age using the figure from Thornley et al. (2000). This is consistent with the prediction that the stars have formed in-situ and were not simply dragged from the outer regions of the parent galaxy during a tidal interaction.

The $[\text{S IV}]/[\text{S III}]$ line ratio is another excitation diagnostic. In M 82 this ratio is 0.05 (Verma et al. 2003), compared to 0.48 ± 0.02 and 0.23 ± 0.05 in TDG-N and TDG-S, respectively. Verma et al. (2003) plotted the log of the $[\text{Ne III}]/[\text{Ne II}]$ against the log of the $[\text{S IV}]/[\text{S III}]$ line ratio for a sample of twelve starburst and blue compact dwarf (BCD) galaxies. Starbursts tend to occupy the bottom left quadrant of the plot, having low excitation. The upper right quadrant is filled with BCDs and galaxies exhibiting Wolf-Rayet features. The corresponding ratios for TDG-N and TDG-S place them in the upper right quadrant with moderate excitation. The $[\text{S IV}]/[\text{S III}]$ line ratio in TDG-N is close to the value for the overlap region in the interacting galaxy pair NGC 4038/NGC 4039, but the $[\text{Ne III}]/[\text{Ne II}]$ ratio is a factor two higher (see Figure 4 in Verma et al. 2003). The ratios for TDG-S are lower. The $[\text{S IV}]/[\text{S III}]$ line ratio is similar to the starburst galaxy, NGC 7714 $[\text{S IV}]/[\text{S III}] = 0.20$, but again the $[\text{Ne III}]/[\text{Ne II}]$ ratio is a factor two higher (Brandl et al. 2004).

The $[\text{S III}]_{33}/18.7 \mu\text{m}$ ratio is a sensitive function of electron density in the range $300 - 30,000 \text{ cm}^{-3}$. The $[\text{S III}]_{33} \mu\text{m}$ line is detected in TDG-N though with low signal-to-noise. The $[\text{S III}]$ ratio is 0.7 ± 0.3 , which implies an electron density of $600 \leq n_e \leq 3000 \text{ cm}^{-3}$ (Figure 1 in Rubin et al. 1994). L79 derived a limit of $< 10^3 \text{ cm}^{-3}$ from their optical spectrum, which is consistent with our result derived from infrared lines.

We detect weak H_2 emission in both TDG-N & TDG-S. The 0-0 S(2) $12.28 \mu\text{m}$ and 0-0 S(1) $17.03 \mu\text{m}$ rotational emission lines have low signal-to-noise ($\text{SNR} \geq 3$) in the IRS-SH spectra, but the 0-0 S(3) $9.66 \mu\text{m}$ is also visible in the IRS-SL spectra (see top of Figures 2 & 3), and all lines, except for the 0-0 (S2) line in TDG-S, are detected in the individual spectra from both nod positions, adding weight to the detection of H_2 . The average line profiles are shown in Figures 5 & 6. To derive the mass of warm molecular hydrogen we assume that the emission is optically thin. The critical densities of the low J levels are relatively low ($n_{\text{cr}} < 10^3 \text{ cm}^{-3}$) and we assume that the populations are in LTE. Adopting an ortho to para ratio of 3 we show the excitation diagrams in Figures 7. These are simply the natural logarithm of the number of molecules divided by the statistical weight in the upper

level of each transition versus the energy level. For a single component model the data lies on a straight line and the excitation temperature is the reciprocal of the fit to the slope. The mass is derived from the S (1) line luminosity and the excitation temperature. In the following equations we outline the derivation for the mass of molecular hydrogen. The energy of a given level, J, is

$$E_J = 85kJ(J + 1) \quad (1)$$

where k is the Boltzmann constant. The total mass is

$$M_{Total} = \frac{4}{3}M_o. \quad (2)$$

Here M_o is the mass of gas in the ortho state and

$$M_o = m_{H_2}N_T \quad (3)$$

where m_{H_2} is the molecular mass of H_2 and N_T is the total number of molecules.

$$N_T = \frac{N_J}{f_J} \quad (4)$$

N_J is the number of molecules for the J^{th} state

$$N_J = \frac{L(J)}{A_J\Delta E_J} \quad (5)$$

$L(J)$ is the line luminosity, A_J is the Einstein A coefficient, $\Delta E_J = h\nu_J$, where h is Planck's constant and ν_J is the frequency of the emission line. f_J is the partition function for the J^{th} state

$$f_J = \frac{g_J e^{-\frac{E_J}{kT}}}{\sum_{J', ortho} g_{J'} e^{-\frac{E_{J'}}{kT}}} \quad (6)$$

where T is the excitation temperature and g_J is the statistical weight for a given state.

For TDG-N and TDG-S the temperature is 460 ± 75 K and 400 ± 40 K. The value is slightly higher than the average value of ~ 350 K measured by us for a large sample of ULIRGs. Assuming the primordial helium mass fraction is ~ 0.25 (e.g. Olive & Skillman 2004), we derive a total mass of warm gas of (1.0 ± 0.7) and $(1.5 \pm 0.6) \times 10^5 M_\odot$ in TDG-N and TDG-S, respectively. The 0-0 S(0) limit is consistent with this temperature, but does not rule out a colder, say 155 K component, which would imply a mass of a few $10^6 M_\odot$. In TDG-N and TDG-S the warm gas is less than 0.1 % of the cold gas mass inferred from ^{12}CO (1-0) observations (Braine et al. 2001). The warm gas fraction is very small compared to the typically \sim few percent and higher found in starbursts (Rigopolou et al. 2002).

3.2. Large Scale Distribution of Non-Stellar Emission

Figure 8 shows the stunning false color image of NGC 5291. The 3.6 & 4.5 μm stellar emission is coded blue and green, respectively, and non-stellar 8 μm emission is coded red. TDG-N and TDG-S stand out prominently in red. There is an excellent correspondence between the 8 μm sources and the 24 near-UV bright knots discovered by L79, with all the sources in their Figure 1, which overlap with our areal coverage, detected. Similarly, all of the emission line sources detected by L79,

Maza et al. (1991) and DM98 are visible. Figure 9 shows the individual IRAC band images. The non-stellar emission in these objects almost certainly arises from strong 7.7 μm and 8.6 μm PAH features that fall within the IRAC 8.0 μm filter. It is likely that any additional TDG candidates lie within the projected $\Sigma_{HI} = 1 M_\odot pc^{-2}$ contour overlaid on the dust image (Figure 1). The IRAC flux densities for the sources labelled in Figure 1 are listed in Table 4. A substantial fraction exist in close groups (e.g., #49-51), while knots #36,39,41-43 are arranged along a 30'' (9 kpc) arc-like distribution. The brightest PAH emitters are clearly associated with regions of higher Σ_{HI} in Figure 1, though, as noted by both L79 and M97, there is a tendency to avoid the actual peak. Also note that a clump of faint knots surrounded by extensive and diffuse non-stellar emission lies 80'' northwest of NGC 5291. A number of sources beyond the projected $1 M_\odot/pc^2$ HI distribution also exhibit bright non-stellar emission. Because of the width of the 8.0 μm IRAC filter, knots with bright non-stellar emission but lacking an optical spectral identification that connects them with the system, may be at substantially different red-shifts and not associated with the NGC 5291 system (e.g., DM98 measured red-shifts of 0.07 and 0.2 for sources #54 & #45 in Figure 1). Further observations will be required to confirm their physical connection with the NGC 5291 system.

3.3. Candidate Tidal Dwarf Galaxy Morphology

In non-stellar emission the knots range in size from essentially unresolved ($D \lesssim 2.5''$ or ~ 0.8 kpc) to $\sim 10''$ (3 kpc) in extent. A number of them show interesting structure. Sources #16 and #17, for example, appear to be connected by a ribbon-like bridge in Figure 10, while #47, 49-51 form a close group of irregularly shaped blobs. L79 noted that faint tails could be observed extending up to $\sim 20''$ from several of the brighter knots. These are visible in Figure 10 for TDG-N (#26) & TDG-S (#33). TDG-S (#33) possesses the longest tail at $\sim 38''$ (11 kpc) in projection, with a noticeable brightening in its southernmost extent which curves off to the East. Several large arcs or loops can be seen in the non-stellar images (see Figures 1, 10 & 11). Two are visible ~ 20 and $40''$ southeast of NGC 5291's nucleus and may represent tidal arms emanating from this galaxy. The expected stellar component may be blended with the diffuse emission. Additional wispy non-stellar emission is apparent $\sim 1.3'$ south of NGC 5291 that may be a complex tail from the close pair #47 & 51. While the knots invariably have lower flux densities at 3.6 μm and 4.5 μm , the more luminous non-stellar sources are also detected in these bands. For example, the heads and tails in TDG-S (#33) and TDG-N (#26) are detected in both stellar 3.6 μm and non-stellar 8 μm emission, as can be seen in Figure 10. However, significant differences can be seen in the stellar and non-stellar structure of knots like #47, 49, 50 - 51 and # 16 & 17. The tails and disturbed morphologies may be signatures of merger events between companion knots.

3.4. NGC 5291 and The Seashell Galaxies

While originally classified as an elliptical, NGC 5291 was re-classified as an S0 galaxy by L79 on the basis of weak spiral structure and a possible dust lane visible in

near-ultraviolet light. Both are consistent with our assessment that the 3.6 and 4.5 μm bands are dominated by cool stars, as in normal galaxies. Figure 11, top-left, shows a closeup of NGC 5291 and the Seashell at 3.6 μm using a logarithmic stretch, and with contours in Figure 11, top-right. NGC 5291 has a bright compact stellar core. A slight twisting of the outer isophotes is apparent, but otherwise the stellar distribution is quite regular. The situation is very different in non-stellar emission, as shown in Figure 11, bottom-left (also with a logarithmic stretch), where NGC 5291 is dominated by a bright and marginally resolved nuclear source ($R \sim 2''$, peak $F_{8.0\mu\text{m}} = 225 \mu\text{Jy arcsec}^{-2}$) and an asymmetric $20''$ (6 kpc) diameter ring ($F_{8.0\mu\text{m}} \sim 36 \mu\text{Jy arcsec}^{-2}$). The ring is highly non-uniform, with two hot-spots north and west of the nucleus and a bifurcation to the southeast. The intensity of the non-stellar emission is also noticeably weaker south and west of the nucleus. Line emission detected by DM98 at a position $8''$ north of NGC 5291's nucleus coincides with this ring. No line emission was detected $4''$ south of the nucleus where Figure 11, bottom-left, shows the non-stellar emission to be considerably weaker. From this we deduce that the ring is actively forming stars, and the non-stellar emission reflects strong PAH features. Whether it is the result of a bar induced resonance (Buta & Combes 1985) or a collision as in the Cartwheel ring galaxy (Higdon 1996) can be determined in principle by detecting expansion using high angular resolution HI observations.

The two faint arcs of non-stellar emission extending $20''$ south of NGC 5291's nucleus in the bottom-left panel in Figure 11 resemble tidal arms seen in other interacting galaxies. There is in addition to these a counter-spray of dust projecting $\sim 40''$ (12 kpc) to the northwest from NGC 5291's nucleus. This can be easily seen in a smoothed version of the non-stellar emission ($5''$ fwhm kernel) in the bottom-right panel of Figure 11, where it coincides with $\Sigma_{\text{HI}} > 5 M_{\odot} \text{pc}^{-2}$ gas in Figure 1 and gradually merges into a fainter and more diffuse non-stellar distribution. Knots of non-stellar emission are also visible in this material, though they are not as bright at 8.0 μm as the majority of the candidate TDGs. The extent of this material suggests a direct connection between NGC 5291 and the TDGs and candidates even in the absence of the HI distribution.

The Seashell displays a highly perturbed stellar morphology at 3.6 μm (Figure 11, top-left), similar to that seen in optical light. This consists of a prominent nucleus and edge-on disk plus two structures extending above the plane, one forming an apparent ring. In non-stellar emission, only the nucleus and edge-on disk components remain, with both much fainter than NGC 5291. This is consistent with its lack of measured HI and line emission (M97; DM98). Also noteworthy is the disk galaxy #5 in Figure 1 (# 435 Richter 1984, M97), located $\sim 4''$ southwest of NGC 5291. Its red color in Figure 8 indicates that it is rich in PAHs with a flocculent spiral structure. This galaxy was classified as an SA(s)c by M97. However a close inspection of the IRAC images shows evidence of a stellar bar and a dusty resonance ring. It shows no signs of either a recent tidal interaction or ram pressure stripping.

3.5. Mid-infrared Spectral Energy Distribution

We now have a detailed understanding of the mid-infrared properties of both TDG-N and TDG-S, which are very similar. Their IRAC SEDs are “notched”, i.e., the flux density falls from 3.6 to 4.5 μm and then steeply rises from 4.5 to 8.0 μm . This spectral shape is characteristic of star forming regions. For an example, see the average 2 - 12 μm Infrared Space Observatory PHT-S spectrum from observations of forty normal galaxies, shown in Figure 3 of Lu et al. (2003). As we are searching for additional candidate TDGs, we use the TDG-N spectrum as our template star forming galaxy. To characterize all the sources listed in Table 5, each SED is compared to a series of template spectra, all normalized at 3.6 μm . Including TDG-N the templates are an S0 (Devriendt, Guiderdoni & Sadat, R. 1999) an elliptical (Silva et al. 1998) and the narrow line Seyfert 1, I Zw 1 from Weedman et al. (2005) as an AGN template. The 3.6 - 5 μm portion of the AGN template is an extension of the continuum to the IRS 5 - 38 μm spectrum. These templates encompass the observed range of IRAC SEDs and the closest match is used to classify each source in Table 4. For TDG-N and TDG-S we measured the near-infrared J, H and Ks flux densities using a $19.5''$ diameter aperture on the 2MASS images (Cutri et al. 2003). For TDG-S (# 33) we quote a $5\text{-}\sigma$ upper limit for the H-band magnitude. To match the extended wavelength coverage of these two TDGs we included the ISO-SWS spectrum of the nucleus of the starburst galaxy M 82 (Lutz et al. 1998) with additional J, H and Ks photometry from the 2MASS images matched to the ISO-SWS aperture. TDG-S shows evidence of a 1.6 μm “bump” from evolved stars, whereas the near infrared emission is flatter in TDG-N and a closer match to M 82, which is shown as a dotted line Figure 12 (dark blue line in electronic edition). The near-infrared component is likely from a combined population of evolved and low-mass main sequence stars. Figure 12 shows example matches for all our templates³. There are 15 objects within the ring (including TDG-N) whose SEDs are well fit by TDG-N (# 15, 17, 18, 19, 25, 26/TDG-N, 32, 33/TDG-S, 36, 39, 41, 42, 47, 49, 50). These are our candidate TDGs. An additional 7 sources in the ring resemble the TDG-N template, but with weaker PAH emission (# 5, 13, 22, 28, 30, 43, 51). These sources are identified as star forming regions in Table 4. Source # 5 is the spiral galaxy SE of NGC 5291 coincident with the HI ring. Our results show that 61 % of the knots identified in the HI ring have mid-infrared SEDs consistent with a young stellar population with 41 % identified as candidate TDGs. If the spectral shape of the candidate TDGs match that of TDG-N and TDG-S both at shorter and longer wavelengths, then the near-infrared will probe the evolved and low-mass main sequence stellar population and the mid-infrared will reveal a population of sources lacking a dominant cool 40 - 60 K dust component.

Three sources outside the ring (# 45, 54 & 59) are a good match to the TDG-N template. These include the two known background starburst galaxies in DM97 (# 54 & #45). Two sources (#64, 66) are a reasonable match to TDG-N. Being outside of the projected HI, these five

³ SED matches for the full sample are given at <http://isc.astro.cornell.edu/~sjuh/tgd/NGC5291/>

sources are listed as star forming regions. Some sources are a poor match to TDG-N but have “notched” SEDs indicating some star formation. NGC 5291’s (#44) SED matches the S0 template, while the Seashell’s (#35) SED is consistent with both an elliptical and S0 template. Source #20 is an elliptical galaxy. A number of sources, #14, 23, 24, 38, 52, 53, 57, 60, 65, 69, may be elliptical galaxies or foreground stars, and #2, 9, 10, 21, 61 may be S0 galaxies or foreground stars. These are labelled E* and S* respectively, in Table 4. Outside of the projected HI ring there are a 7 sources that may be background AGN as their SEDs can be fit with a simple power law (#3, 4, 6, 8, 12 56 73).

The number of sources located inside and outside the projected HI ring are roughly equal, but the ring has only $\sim 40\%$ the areal coverage of the background. 44% of the sources located within the ring are good matches to the TDG-N SED compared to 8% of the sources located outside the ring. To estimate the sample contamination we assume that the three good matches to TDG-N that lie outside the HI ring are from foreground/background sources. From this number we infer that approximately two of the candidate TDGs may not be associated with the NGC 5291 system.

3.6. Color Magnitude and Color-Color Relations

In this section we look at the color-color and color-magnitude plots to see whether TDG-N, TDG-S and the thirteen candidate TDGs occupy a distinct region of color-color/magnitude space when compared to other galaxy types. In Figure 13 we plot the $[4.5] - [8.0]$ versus $[3.6] - [4.5]$ color. The vertical and horizontal lines mark the color zero-points, using the zero-point flux densities listed in §2.2. The plot is now divided into four quadrants. A source with a flat SED would lie at the crossing point. Sources in the lower left quadrant have falling SEDs typical of E and S0 galaxies like the Seashell and NGC 5291 (see # 35 & 44 in Figure 12). AGN-like sources, for example, #12a shown in Figure 12, with rising SEDs are located in the upper right quadrant. The lower right quadrant contains sources with active star formation. The candidate TDGs, for example, see #26, 33 & 42 in Figure 12, are plotted with a framed-diamond symbol. They have $[4.5] - [8.0] > 3.2$ and $[3.6] - [4.5] < 0.4$. Sources which are a reasonable match to TDG-N, for example see #13 in Figure 12, but with weaker $8\ \mu\text{m}$ emission and therefore not included in our candidate TDG list, are plotted as double diamonds. Sources which are a good match to TDG-N, but lie outside the projected HI ring, are plotted as solid diamond symbols. The remaining “notched” SED sources in this quadrant, for example, see #48a in Figure 12, are a poor match to TDG-N and are shown as open-diamond symbols.

For comparison the sample of 18 galaxies from Pahre et al. (2004) are plotted as crosses. This sample contains representative galaxies from the Hubble morphological sequence and spans E1 through IB(s)m galaxies. The candidate TDGs do not overlap with this sample. The late type galaxy NGC 5669 has the reddest $[4.5] - [8.0]$ color of 2.7 in the Pahre et al. (2004) sample, as compared to the average value of 3.8 for the candidate TDGs. Also included in Figure 13 are the 19 BCD galaxies from the KPNO International Spectroscopic Survey (KISS), observed with IRAC by Rosenberg et al. (2005). These

sources, shown as filled circles, were selected from the KPNO International Spectroscopic Survey (KISS, Salzer et al. 2000) conducted in the NDWFS Boötes field (Januzzi & Dey 1999), and span a wide range in metallicity ($7.8 \leq 12 + \log O/H \leq 9.1$) and star formation rate ($0.1 \leq \text{SFR} \leq 2.1\ M_{\odot}\ \text{yr}^{-1}$). Only one BCD (#2316) overlaps with the TDG and candidate TDG distribution. This object is noteworthy for having the highest oxygen abundance and second highest SFR ($1.3\ M_{\odot}\ \text{yr}^{-1}$) among the BCDs. The two next closest BCDs in Figure 13 (#2328 & #2359 in Rosenberg et al. 2005) have the highest and third highest SFRs. Otherwise, their properties (i.e., $H\alpha$ equivalent widths, metallicity) do not distinguish them from the remaining BCD sample. The TDGs and candidate TDGs all show significantly enhanced non-stellar emission, most likely due to PAHs, relative to normal spirals and even BCD galaxies.

In Figure 14 we plot the $[3.6] - [8.0]$ color as a function of the absolute $[8.0]$ magnitude. There is no overlap with the Rosenberg et al. (2004) sample of BCDs. The average for the two TDGs and the 13 candidate TDGs is ~ 1.5 magnitudes redder in $[3.6] - [8.0]$ color and ~ 1.9 magnitudes fainter at $8\ \mu\text{m}$. The TDGs and candidate TDGs have a very narrow range in $[3.6] - [8.0]$ color of 0.7 compared to the BCD sample, which has a spread of 2.5.

3.7. Stellar Masses For The Candidate TDGs

A widely used technique for determining the stellar mass distributions in disk galaxies is to multiply the measured broadband luminosity by the appropriate mass-to-luminosity ratio (van Albada et al. 1985). This is generally best carried out at near-infrared wavelengths, where the effects of dust and massive stars are minimized (Kranz et al. 2001; Verheijen 2001). Adopting this approach, we estimated the stellar masses for TDG-N & TDG-S by first calculating their luminosities in the K_s -band, defined as $L_{K_s} = 4\pi d^2 \nu F_{\nu}$ with $\nu = 1.4 \times 10^{14}$ Hz. Expressed in terms of the sun’s K_s -band luminosity ($L_{\odot, K_s} = 5.3 \times 10^{25}$ W), this can be written as

$$L_{K_s} = 3.3 \times 10^{-37} d^2 F_{K_s} (L_{\odot, K_s}), \quad (7)$$

where d is the distance in meters and F_{K_s} is the flux density in Janskys. For TDG-N & TDG-S we found $L_{K_s} = (3.4 \text{ and } 6.3) \times 10^8 L_{\odot, K_s}$, respectively. Stellar masses were obtained by multiplying these luminosities by K_s -band mass-to-luminosity ratios (M_*/L_{K_s}) calculated by Bell & de Jong (2001) for model spiral galaxies. This choice seemed appropriate given that both the metal abundances ($Z \sim 1/3 Z_{\odot}$) and optical colors ($B-R \sim 0.6$) of the candidate TDGs in the NGC 5291 system are similar to those found in the disks of late spiral galaxies (L79; DM98). Bell & de Jong found that their derived M_*/L depended on the optical color, as was expected. However, the color dependence is minimized in the near-infrared. For a $B - R = 0.6$, their models give $M_*/L_K = 0.3-0.6\ M_{\odot}/L_{\odot, K_s}$. Using these values results in a stellar mass of $1.5 \pm 0.6 \times 10^8\ M_{\odot}$ for TDG-N, which is consistent with Bournaud et al.’s (2004) estimate obtained from its blue luminosity and a M/L_B of two. For TDG-S we derive a stellar mass of $3.0 \pm 1.0 \times 10^8\ M_{\odot}$. These are roughly 10% the stellar mass of the LMC (Leroy et al. 2005).

We also estimated stellar masses for the thirteen candidate TDGs in Table 4 showing evidence of strong PAH emission like TDG-N & TDG-S. These are the framed-diamond symbol sources in Figures 13 and 14. Since none of these sources were detected by 2MASS at J, H, or K_s , we calculated F_{K_s} flux densities from their 3.6 μm data using the mean ($K_s - [3.6]$) color index for TDG-N & TDG-S, which is 0.9 ± 0.5 . For these sources, F_{K_s} in the above equation was replaced with $F_{3.6\mu\text{m}} \times 10^{-0.4 \times 0.9} \times (645./277.5)$, where the last factor takes into account the different zero points in the two bands. We derive a mean K_s luminosity and stellar mass of $4 \pm 2 \times 10^7 L_\odot$, K_s and $2 \pm 1 \times 10^7 M_\odot$ respectively for these sources, with the largest source of uncertainty arising from the observed spread in $K_s - [3.6]$ color. TDG candidate #32 ($\sim 1'$ southeast of TDG-N) is the most massive of this group with $M_* = 6 \pm 3 \times 10^7 M_\odot$. Defined this way, TDG-N & TDG-S possess stellar masses that are roughly an order of magnitude larger than the average for the thirteen other candidate TDGs of the HI ring with $[4.5]-[8.0] > 3.2$.

In a similar way, we estimated stellar masses for the nineteen BCD galaxies from Rosenberg et al. (2005). Four of the BCDs were detected at K_s as well, and their average $K_s - [3.6]$ color (1.0 ± 0.5) is similar to the mean for TDG-N & S, with a comparable spread in value. For these galaxies we either calculated L_\odot , K_s and M_* directly from their K_s -band flux densities, or indirectly using their 3.6 μm flux densities and mean $K_s - [3.6]$ color. For the latter fifteen objects, the largest source of uncertainty in the $K_s - [3.6]$ colors, which we take to be the observed spread among the four BCDs detected at K_s -band. On average, the BCDs have considerably larger stellar masses than the TDG-candidate population associated with NGC 5291, with a median $M_* = 6 \pm 3 \times 10^8 M_\odot$. TDG-N & TDG-S are close to this average value, however the other TDG-candidates have stellar masses roughly an order of magnitude smaller than the typical BCD in Rosenberg et al.'s KISS sample. These objects are detected to considerably larger distances than NGC 5291, leading to a possible Malmquist bias. However, we find a nearly identical median stellar mass for the Rosenberg et al. sample if we restrict ourselves to those BCDs within 125 Mpc, which is the distance where our faintest TDG-candidate would have been detected in all four IRAC bands at 5σ . Of the sources in Table 4, only TDG-N & TDG-S appear to have stellar masses expected for a typical BCD.

4. CONCLUSIONS

We have presented mid-infrared spectra of two tidal dwarf galaxies, TDG-N & TDG-S in the NGC 5291 system. Both are PAH rich with features at 6.2, 7.7, 8.6, 11.3 and 16.5 μm . The 5 - 14 μm spectra are remarkably similar in shape to both the starburst galaxy M 82 and the reflection nebula NGC 7023. However, detailed examination reveals their differences. The relative PAH strengths are indicative of an equal mix of ionized and neutral PAHs, with groups of ~ 100 carbon atoms, as opposed to the almost totally ionized PAHs present in the starburst galaxy M 82. The rise in flux density (F_ν) flattens off around 20 μm in both TDG-N and TDG-S and the spectra can be fit with a $T \sim 140$ K dilute blackbody.

This is in marked contrast with many spiral and starburst galaxies, such as M 82, whose spectra peak around 60 - 100 μm due to a dominant cooler dust component with a temperature ~ 40 K. In TDG-N the 1.6 μm bump from an evolved stellar population is absent. Both TDG-N and TDG-S are dominated by young stellar populations. Their spectra exhibit many fine structure and molecular lines allowing us to calculate the physical properties of the star forming regions. The electron density derived from the [S III] ratio in TDG-N is $600 \leq n_e \leq 3000 \text{ cm}^{-3}$. Both the [S IV]/[S III] and [Ne III]/[Ne II] ratios are higher than typical ratios measured in starburst galaxies and closer to the values measured for BCD and Wolf-Rayet galaxies. Both metallicity and the age of a starburst effect the level of excitation. The TDGs' have one-third solar metallicity and the [Ne III]/[Ne II] line ratios are consistent with models that have the most recent epoch of star formation occurring less than five million years ago. This results in a moderately high excitation. The age of the starburst is consistent with models which predict that the young stars have formed in-situ and were not part of the parent galaxy.

For the first time we have the sensitivity to measure the low J rotational lines from molecular hydrogen and thereby make a direct measurement of the warm molecular mass. Assuming the gas is in LTE with an ortho-para ratio of 3, we derive temperatures of 460 ± 75 K and 400 ± 40 K, with a corresponding mass of warm gas of (1.0 ± 0.7) and $(1.5 \pm 0.6) \times 10^5 M_\odot$ in TDG-N and TDG-S, respectively. This warm mass is $< 0.1\%$ of the cold gas mass inferred from ^{12}CO (1-0) measurements.

IRAC observations have identified 13 additional sources within the HI ring that resemble TDG-N and TDG-S. These candidate TDGs occupy a distinct region of IRAC color space with $[3.6] - [4.5] < 0.4$ and $[4.5] - [8.0] > 3.2$ as compared to elliptical, spiral, irregular and BCD galaxies, which tend to have $[4.5] - [8.0] < 3.2$. The combined TDG and candidate TDG sample has a very narrow dispersion in $[3.6] - [8.0]$ color of ~ 0.7 , unlike a sample of BCDs, which has a spread of ~ 2.5 . Compared to the BCDs the average candidate TDG is ~ 1.5 magnitudes redder with an $[3.6] - [8.0]$ color of 3.6 and ~ 1.9 magnitudes fainter at 8 μm , with an absolute magnitude of ~ -21.6 . Approximately 40% of the knots identified in the HI ring fit the TDG template with strong PAH 7.7 & 8 μm emission a factor ~ 6 times the luminosity of the cool stellar population. Using their 2MASS K_s -band flux densities and a starburst M_*/L_{K_s} appropriate for their B-R colors, we derive stellar masses of (1.5 ± 0.6) and $(3.0 \pm 1.0) \times 10^8 M_\odot$ for TDG-N and TDG-S respectively. These values are comparable to similarly defined stellar masses for a sample of BCDs, though still only $\sim 10\%$ of the LMC's stellar mass. Adopting a mean $K_s - [3.6]$ color of 0.9 for the remaining candidate TDGs, we used their 3.6 μm luminosities to derive stellar masses from $0.8-6.0 \times 10^7 M_\odot$.

The IRAC images of the HI ring show an incredibly rich nursery for star formation. Many of the candidate TDGs have a disturbed morphology possibly resulting from previous tidal encounters with fellow companions. These are new star forming systems and may be local analogues of star formation resulting from tidal interactions in the early universe.

Future work will compare this population of TDGs with our Spitzer sample of TDG systems, which includes observations of Stephan's Quintet, Arp 245 and Arp 105.

We thank the referee, John Hibbard, for his very careful reading of our manuscript and good suggestions. We thank Dr. M. Ashby for many useful conversations concerning IRAC data analysis. We thank Prof. M. Haynes for many helpful discussions and encouragement. We thank Prof. J. R. Houck for the allocation of valuable IRS guaranteed time to the TDG program. This work is based [in part] on observations made with the Spitzer Space Telescope, which is operated by the Jet Propulsion Laboratory, California Institute of Technology under NASA contract 1407. Support for this work was provided by NASA through Contract Number 1257184 issued by

JPL/Caltech. This research has made use of the excellent NASA/IPAC Extragalactic Database (NED) which is operated by the Jet Propulsion Laboratory, California Institute of Technology, under contract with the National Aeronautics and Space Administration; data products from the Two Micron All Sky Survey, which is a joint project of the University of Massachusetts and the Infrared Processing and Analysis Center/California Institute of Technology, funded by the National Aeronautics and Space Administration and the National Science Foundation; the SIMBAD database; and archival data from the National Radio Astronomy Observatory, which is a facility of the National Science Foundation operated under cooperative agreement by Associated Universities, Inc.

REFERENCES

- van Albada, T. S., Bachall, J. N., Begeman, K. & Sancisi, R. 1985, *ApJ*, 295, 305
- Bell, E. F. & de Jong, R. S. 2001, *ApJ*, 550, 212
- Bertin, E. & Arnouts, S. 1996, *A&AS*, 117, 393
- Bournaud, F., Duc, P.-A., Amram, P., Combes, F. & Gach, J. -L. 2004, *A&A* 425, 813
- Braine, J., Duc, P.-A., Lisenfeld, U., Charmandaris, V. Vallejo, O., Leon, S. & Brinks, E. 2001, *A&A*, 378, 51
- Brandl et al., 2004 *ApJS*, 154, 188
- Buta, R. J. & Combes, F. 1996, *Fundam. Cosmic Physics*, 17, 95
- Cohen, M., Megeath, T.G., Hammersley, P.L., Martin-Luis, F., & Stauffer, J. 2003, *AJ*, 125, 2645
- Cutri, R. et al. 2003, 2MASS All-Sky Catalog of Point Sources, VizieR On-line Data Catalog: II/246. Originally published in: University of Massachusetts and Infrared Processing and Analysis Center, (IPAC/California Institute of Technology) (2003)
- Devriendt, J. E. G., Guiderdoni, B., & Sadat, R. 1999, *A&A*, 350, 381
- Draine, B. T. & Li, A. 2001, *ApJ*, 551, 807
- Duc, P.-A. & Mirabel, I. F., 1998 *A&A*, 333, 813 (DM98)
- Eisenhardt, P. R. et al. 2004, *ApJS*, 154, 48
- Elmegreen, B. G., Kaufman, M. & Thomasson, M. 1993, *ApJ*, 412, 90
- Fazio, G. G. et al., 2004 *ApJS*, 154, 10
- Hibbard, J. E. & van Gorkom, J. H. 1996, *AJ*, 111, 655
- Hibbard, J. E. & Mihos, J. C. 1995, *AJ*, 110, 140
- Higdon, J. L. 1996, *ApJ*, 467, 241
- Higdon, S. J. U. et al. 2004, *PASP*, 116, 975
- Houck, J. R. et al., 2004a *ApJS*, 154, 18
- Houck, J. R. et al., 2004b *ApJS*, 154, 211
- van der Hulst, J. M. 1979, *A&A*, 71, 131
- Hunsberger, S. D., Charlton, J., & Zaritsky, D. 1996, *ApJ*, 462, 50
- Jannuzi, B. & Dey, A. 1999, *ASP Conference Series* Vol. 191, (R. Weymann, L. Storrie-Lombardi, M. Sawicki, & R. Brunner, eds.), p. 111
- Kranz, T., Slyz, A. & Rix, H. 2001, *ApJ*, 562, 164
- Leroy, A., Bolatto, A. D., Simon, J. D., & Blitz, L. 2005, *ApJ*, 625, 763
- Longmore, A. J., Hawarden, T. G., Cannon, R. D., Allen, D. A., Mebold, U., Goss, W. M., & Reif, K. 1979 *MNRAS*, 188, 285 (L79)
- Lu, N. et al. 2003, *ApJ*, 588, 199
- Lutz, D., Genzel, R., Kunze, D., Spoon, H. W. W., Sturm, E., Sternberg, A. & Moorwood, A. F. M. 1998, In: *ASP Conf. Ser.* 132, Starformation with the Infrared Space Observatory. p.89
- Malphrus, B. K., Simpson, C. E., Gottesman, S. T. & Hawarden, T. G. 1997, *AJ*, 114, 1427 (M97)
- Mateo, M. L. 1998, *ARA&A*, 36, 435
- Maza, J., Ruiz, M. T., Pena, M., Gonzalez, L. & Wischnjewsky, M. 1991, *A&A Suppl.*, 89, 389
- Mirabel, I. F., Lutz, D., & Maza, J. 1991, *A&A*, 243, 367
- Olive, K. A. & Skillman, E. D. 2004, *ApJ*, 617, 29
- Pahre, M. A., Ashby, M. L. N., Fazio, G. G. & Willner, S. P. 2004, *ApJS*, 154, 235
- Pedersen, H., Gammelgaard, P. & Lausten, S. 1978, *The Messenger*, 13, 11
- Pena, M., Ruiz, M. T. & Maza, J. 1991, *A&A*, 251, 417
- Pfenniger, D., Combes, F. & Martinet, L. 1994, *A&A*, 285, 79
- Richter, O. -G. 1984, *A&AS*, 58, 131
- Rosenberg, J. L., Ashby, M. L. N., Salzer, J. J. & Huang, J. -S. 2005, *ApJ*, submitted.
- Rubin, R. H., Simpson, J. P., Lord, S. D., Colgan, W. J., Erickson, E. F. & Haas, M. R. 1994, *ApJ*, 420, 772
- Salzer, J. J. et al. 2000, *AJ*, 120, 80
- Sanders, D. B. & Mirabel, I. F. 1996, *ARAA*, 34, 749
- Schweizer, F. 1978, *IAU Symposium* 77, Structure and Properties of Nearby Galaxies, p. 279.
- Silva, L., Granato, G., Bressan, A. & Danese, L. 1998, *ApJ*, 509, 103
- Schombert, J. M., Wallin, J. F. & Struck-Marcell, C. 1990, *ApJ*, 99, 497
- Thornley, M. D., Forster Schreiber, M., Lutz, D. Genzel, R. Spoon, H. W. W. & Kunze, D. 2000, *ApJ* 539 641
- Toomre, A. & Toomre, J. 1972, *ApJ*, 178, 623
- Verheijen, M. A. 2001, *ApJ*, 563, 694.
- Verma, A. Lutz, D., Sturm, E., Sternberg, A., Genzel, R. & Vacca, W. 2003, *A&A*, 403, 829
- Werner, M. W., et al. 2004a, *ApJS*, 154, 1
- Werner, M. W., Uchida, K. I., Sellgren, K., Marengo, M., Gordon, K. D., Morris, P. W., Houck, J. R. & Stansberry, J. A. 2004b, *ApJS*, 154, 309
- Weedman, D. W. et al., 2005, *ApJ*, Submitted.
- Zwicky, F. 1956, *Ergebnisse der Exakten Naturwissenschaften*, 29, 344

TABLE 1
OBSERVATIONAL PARAMETERS

Object	RA (J2000) h:m:s	Dec (J2000) d:m:s	Date	Instrument	Integration (s)	Execution Time (min)
NGC5291	13:47:23.00	-30:25:30.00	2004-02-17	IRAC	3×12	44.87
TDG-N	13:47:20.50	-30:20:51.00	2004-07-17	IRS		77.81
				IRS-SL1	60×4	
				IRS-SL2	60×4	
				IRS-SH	60×4	
				IRS-LH	120×7	
TDG-S	13:47:23.00	-30:27:30.00	2004-07-17	IRS		77.73
				IRS-SL1	60×4	
				IRS-SL2	60×4	
				IRS-SH	60×4	
				IRS-LH	120×7	

TABLE 2
PAH FLUX

$\lambda_{central}$ (μm)	Flux ($10^{-21} \text{ Wcm}^{-2}$)	EW (μm)	PAH _x /PAH7.7
TDG-N			
6.2	$13.2^{+1.4}_{-1.4}$	$-5.9^{+0.7}_{-0.7}$	$0.35^{+0.06}_{-0.06}$
7.7	$37.2^{+5.2}_{-5.2}$	$-12.0^{+1.4}_{-1.4}$	1.00
8.6	$8.1^{+1.3}_{-1.3}$	$-2.1^{+0.4}_{-0.4}$	$0.22^{+0.05}_{-0.05}$
11.3	$8.1^{+0.6}_{-0.6}$	$-1.7^{+0.2}_{-0.2}$	$0.22^{+0.03}_{-0.03}$
12.0	$1.8^{+0.6}_{-0.6}$	$-0.4^{+0.2}_{-0.2}$	$0.05^{+0.02}_{-0.02}$
12.6	$5.7^{+1.2}_{-1.2}$	$-1.3^{+0.3}_{-0.3}$	$0.15^{+0.04}_{-0.04}$
13.5	$1.5^{+0.5}_{-0.5}$	$-0.4^{+0.1}_{-0.1}$	$0.04^{+0.01}_{-0.01}$
16.5 ^a	$0.6^{+0.2}_{-0.2}$	$-0.01^{+0.01}_{-0.01}$	$0.02^{+0.01}_{-0.01}$
TDG-S			
6.2	$3.3^{+1.0}_{-1.0}$	$6.8^{+2.1}_{-2.1}$	$0.33^{+0.11}_{-0.11}$
7.7	$10.0^{+1.3}_{-1.3}$	$12.3^{+1.8}_{-1.8}$	1.00
8.6	$2.6^{+0.7}_{-0.7}$	$2.5^{+0.7}_{-0.7}$	$0.27^{+0.08}_{-0.08}$
11.3	$2.3^{+0.1}_{-0.1}$	$1.54^{+0.30}_{-0.30}$	$0.23^{+0.05}_{-0.05}$
12.0	$0.6^{+0.2}_{-0.2}$	$0.4^{+0.2}_{-0.2}$	$0.06^{+0.03}_{-0.03}$
12.6	$1.2^{+0.4}_{-0.4}$	$0.8^{+0.3}_{-0.3}$	$0.12^{+0.04}_{-0.04}$
13.5	$0.10^{+0.06}_{-0.06}$	$0.1^{+0.1}_{-0.1}$	$0.01^{+0.01}_{-0.01}$
16.5 ^a	$1.0^{+0.5}_{-0.5}$	$-0.03^{+0.02}_{-0.02}$	$0.10^{+0.05}_{-0.05}$

^aFrom the IRS-SH aperture, uncertainty includes aperture scaling factor between IRS-SL and IRS-SH.

TABLE 3
LINE FLUXES

Line	TDG-N Line Flux ($10^{-22} \text{ Wcm}^{-2}$)	EW (μm)	TDG-S Line Flux ($10^{-22} \text{ Wcm}^{-2}$)	EW (μm)
[S IV] 10.51 μm	$7.40^{+0.15}_{-0.15}$	$-0.018^{+0.002}_{-0.002}$	$1.05^{+0.22}_{-0.22}$	$-0.002^{+0.001}_{-0.001}$
[Ne II] 12.81 μm	$10.65^{+0.06}_{-0.06}$	$-0.024^{+0.001}_{-0.001}$	$4.05^{+0.31}_{-0.31}$	$-0.011^{+0.003}_{-0.003}$
[Ne III] 15.56 μm	$25.31^{+1.03}_{-1.03}$	$-0.065^{+0.002}_{-0.002}$	$5.47^{+0.11}_{-0.11}$	$-0.016^{+0.002}_{-0.002}$
[S III] 18.71 μm	$15.45^{+0.58}_{-0.58}$	$-0.041^{+0.002}_{-0.002}$	$4.66^{+0.17}_{-0.17}$	$-0.015^{+0.000}_{-0.000}$
[S III]	$10.61^{+4.02}_{-4.02}$	$-0.100^{+0.049}_{-0.049}$	$\leq 37.87^{+0.54}_{-0.54}$...
0-0 S(3) 9.66 ^a	$2.2^{+0.9}_{-0.9}$	$-0.04^{+0.02}_{-0.02}$	$1.6^{+0.5}_{-0.5}$ ^b	$-0.08^{+0.03}_{-0.03}$
0-0 S(2) 12.28	$1.9^{+0.8}_{-0.8}$	$-0.003^{+0.001}_{-0.001}$	$0.9^{+0.4}_{-0.4}$ ^c	$-0.002^{+0.001}_{-0.001}$
0-0 S(1) 17.03	$1.1^{+0.4}_{-0.4}$	$-0.003^{+0.001}_{-0.001}$	$1.3^{+0.3}_{-0.3}$ ^d	$-0.002^{+0.001}_{-0.001}$
0-0 S(0) 28.22	≤ 1.7 ^d	...	≤ 1.7 ^e	...

^aIRS-SL

^bFWHM fixed to instrumental resolution of 0.088 μm .

^cFWHM fixed to instrumental resolution of 0.020 μm .

^dFWHM fixed to instrumental resolution of 0.028 μm .

^e3- σ upper limit. Calculated using a 0-order fit to the continuum. The upper limit is $3 \times \text{RMS} \times \text{FWHM}$. The FWHM is 0.05 μm .

TABLE 4
IRAC FLUX DENSITIES IN AN 8 PIXEL DIAMETER APERTURE

Object ^a		RA (J2000) (^o)	Dec (J2000) (^o)	F _{3.6μm}} (μ Jy)	F _{4.5μm}} (μ Jy)	F _{5.8μm}} (μ Jy)	F _{8.0μm}} (μ Jy)
1	AGN	206.77913	-30.463076	82.6 ⁺ 3.5	67.6 ⁺ 3.4	73.2 ⁺ 15.2	67.1 ⁺ 10.3
2 ^b	S0*	206.78200	-30.411720	220.0 ⁺ 3.5	201.0 ⁺ 3.4	104.0 ⁺ 15.2	107.0 ⁺ 10.3
3 ^b	AGN	206.78366	-30.425823	114.0 ⁺ 3.5	123.0 ⁺ 3.4	167.0 ⁺ 15.2	147.0 ⁺ 10.2
4 ^b	AGN	206.80237	-30.392924	126.0 ⁺ 2.6	175.0 ⁺ 2.9	268.0 ⁺ 10.9	365.0 ⁺ 9.2
5 ^{cd}	SF	206.80253	-30.456886	5460.0 ⁺ 20.2	3390.0 ⁺ 18.1	6200.0 ⁺ 65.4	16500.0 ⁺ 55.3
6 ^b	AGN	206.80267	-30.439257	188.0 ⁺ 3.5	343.0 ⁺ 3.4	614.0 ⁺ 15.2	1240.0 ⁺ 10.3
7 ^b	N	206.80351	-30.363409	52.0 ⁺ 3.5	33.2 ⁺ 3.4	70.1 ⁺ 14.9	62.3 ⁺ 10.3
8 ^b	AGN	206.80364	-30.372922	66.8 ⁺ 3.5	97.1 ⁺ 3.4	206.0 ⁺ 15.2	240.0 ⁺ 10.3
9	S0*	206.80908	-30.468743	107.0 ⁺ 3.5	74.8 ⁺ 3.4	79.5 ⁺ 15.2	61.6 ⁺ 10.3
10 ^b	S0*	206.81047	-30.420336	169.0 ⁺ 3.5	122.0 ⁺ 3.4	90.8 ⁺ 15.2	77.0 ⁺ 10.3
11	AGN?	206.82215	-30.339189	112.0 ⁺ 3.5	112.0 ⁺ 3.4	301.0 ⁺ 14.3	161.0 ⁺ 10.0
12 ^b	AGN	206.82216	-30.414722	35.2 ⁺ 2.6	44.0 ⁺ 2.9	60.2 ⁺ 10.9	100.0 ⁺ 9.2
13	H - SF	206.82294	-30.472132	140.0 ⁺ 3.5	107.0 ⁺ 3.4	170.0 ⁺ 15.2	419.0 ⁺ 10.2
14	E*	206.82355	-30.453369	204.0 ⁺ 3.5	127.0 ⁺ 3.4	71.6 ⁺ 15.2	51.0 ⁺ 10.2
15	- f TDG	206.82406	-30.366257	39.9 ⁺ 3.5	29.1 ⁺ 3.4	86.6 ⁺ 15.2	252.0 ⁺ 10.2
16	N	206.82418	-30.356122	145.0 ⁺ 3.5	122.0 ⁺ 3.4	92.3 ⁺ 15.2	231.0 ⁺ 10.2
17	- h TDG	206.82499	-30.352538	89.9 ⁺ 3.5	57.1 ⁺ 3.4	259.0 ⁺ 15.2	663.0 ⁺ 10.2
18	TDG	206.82504	-30.364186	45.0 ⁺ 3.5	24.8 ⁺ 3.4	130.0 ⁺ 15.2	352.0 ⁺ 10.3
19	TDG	206.82672	-30.344119	30.7 ⁺ 3.5	9.6 ⁺ 3.4	< 36.3	188.0 ⁺ 10.2
20 ^b	1 C E	206.82682	-30.383323	1050.0 ⁺ 6.5	625.0 ⁺ 6.2	341.0 ⁺ 28.0	246.0 ⁺ 18.5
21	S0*	206.82883	-30.452879	207.0 ⁺ 3.5	133.0 ⁺ 3.4	93.7 ⁺ 15.2	75.0 ⁺ 10.2
22	- b SF	206.83111	-30.448559	49.5 ⁺ 2.6	32.1 ⁺ 2.9	40.7 ⁺ 10.8	106.0 ⁺ 9.2
23	E*	206.83137	-30.415181	243.0 ⁺ 3.5	167.0 ⁺ 3.4	118.0 ⁺ 15.2	73.0 ⁺ 10.3
24	E*	206.83159	-30.399068	471.0 ⁺ 3.5	316.0 ⁺ 3.4	224.0 ⁺ 15.2	101.0 ⁺ 10.2
25	A j TDG	206.83236	-30.339936	69.3 ⁺ 2.6	38.0 ⁺ 2.9	402.0 ⁺ 10.8	486.0 ⁺ 9.2
26 ^{de}	B i TDG	206.83508	-30.347620	513.0 ⁺ 6.5	389.3 ⁺ 6.2	1844.5 ⁺ 28.2	4804.0 ⁺ 18.8
27	N	206.83516	-30.447661	80.7 ⁺ 2.6	56.6 ⁺ 2.9	28.9 ⁺ 10.8	76.4 ⁺ 9.2
28	SF	206.83619	-30.445187	19.8 ⁺ 2.6	8.1 ⁺ 2.9	18.9 ⁺ 10.9	71.1 ⁺ 9.3
29		206.83759	-30.384396	<11.7	<9.0	26.9 ⁺ 10.8	85.2 ⁺ 9.2
30	4 - SF	206.83873	-30.472597	373.0 ⁺ 3.5	256.0 ⁺ 3.4	286.0 ⁺ 15.2	1350.0 ⁺ 10.3
31		206.84210	-30.383212	8.9 ⁺ 2.6	10.4 ⁺ 2.9	52.3 ⁺ 10.9	158.0 ⁺ 9.2
32	- g TDG	206.84312	-30.362525	118.0 ⁺ 3.5	72.5 ⁺ 3.4	300.0 ⁺ 15.2	853.0 ⁺ 10.2
33 ^{df}	F a TDG	206.84521	-30.458553	295.0 ⁺ 6.5	160.9 ⁺ 6.1	617.8 ⁺ 28.2	1930.0 ⁺ 18.8
34 ^b	AGN?	206.84561	-30.491370	92.7 ⁺ 3.5	80.8 ⁺ 3.4	78.2 ⁺ 15.2	111.0 ⁺ 10.3
35 ^{gh}	- B E S0	206.84707	-30.417140	17500.0 ⁺ 21.2	10400.0 ⁺ 19.9	8050.0 ⁺ 72.0	6110.0 ⁺ 54.7
36	TDG	206.84741	-30.449865	27.4 ⁺ 2.6	17.8 ⁺ 2.9	28.4 ⁺ 10.9	174.0 ⁺ 9.2
37 ^b	AGN?	206.84765	-30.489807	61.1 ⁺ 2.6	59.6 ⁺ 2.9	48.7 ⁺ 10.8	72.1 ⁺ 9.2
38	E*	206.84767	-30.357765	895.0 ⁺ 3.5	578.0 ⁺ 3.4	432.0 ⁺ 15.2	227.0 ⁺ 10.3
39	TDG	206.84773	-30.447670	17.1 ⁺ 2.6	15.0 ⁺ 2.9	27.3 ⁺ 10.8	113.0 ⁺ 9.3
40 ^b	AGN?	206.84823	-30.345555	51.4 ⁺ 3.5	79.7 ⁺ 3.4	52.3 ⁺ 15.2	101.0 ⁺ 10.2
41	- c TDG	206.84868	-30.445188	25.0 ⁺ 2.6	10.8 ⁺ 2.9	40.0 ⁺ 10.9	137.0 ⁺ 9.2
42	E - TDG	206.84913	-30.452056	51.0 ⁺ 3.5	32.7 ⁺ 3.4	105.0 ⁺ 15.2	258.0 ⁺ 10.2
43	D d SF	206.84915	-30.439878	62.8 ⁺ 2.6	40.5 ⁺ 2.9	62.1 ⁺ 10.9	180.0 ⁺ 9.2
44 ^{gi}	- A E	206.85203	-30.407169	69400.0 ⁺ 41.9	40800.0 ⁺ 36.1	30900.0 ⁺ 87.2	36400.0 ⁺ 88.7
45 ^b	- 2 SF	206.85413	-30.374597	76.0 ⁺ 2.6	62.0 ⁺ 2.9	25.1 ⁺ 10.8	198.0 ⁺ 9.2
46 ^b		206.85697	-30.492522	282.0 ⁺ 3.5	176.0 ⁺ 3.4	71.9 ⁺ 15.2	60.9 ⁺ 10.3
47	TDG	206.85752	-30.430211	38.6 ⁺ 2.6	17.3 ⁺ 2.9	97.6 ⁺ 10.8	284.0 ⁺ 9.2
48 ^b	N	206.85858	-30.395310	205.0 ⁺ 2.6	181.0 ⁺ 2.9	149.0 ⁺ 10.9	290.0 ⁺ 9.2
49	TDG	206.85934	-30.433200	27.5 ⁺ 2.6	15.1 ⁺ 2.9	50.1 ⁺ 10.8	158.0 ⁺ 9.2
50	TDG	206.86013	-30.434832	27.7 ⁺ 2.6	21.0 ⁺ 2.9	57.2 ⁺ 10.8	162.0 ⁺ 9.3
51	C e SF	206.86030	-30.430790	134.0 ⁺ 2.6	88.9 ⁺ 2.9	142.0 ⁺ 10.8	313.0 ⁺ 9.2
52 ^b	E*	206.86159	-30.508598	215.0 ⁺ 3.5	175.0 ⁺ 3.4	121.0 ⁺ 15.2	76.7 ⁺ 10.3
53 ^b	E*	206.86201	-30.359309	268.0 ⁺ 3.5	173.0 ⁺ 3.4	104.0 ⁺ 15.2	75.2 ⁺ 10.3
54 ^b	2 1 54	206.86375	-30.371721	663.0 ⁺ 3.5	446.0 ⁺ 3.4	629.0 ⁺ 15.2	4070.0 ⁺ 10.3
55 ^b		206.86543	-30.447166	115.0 ⁺ 3.5	111.0 ⁺ 3.4	104.0 ⁺ 15.2	64.9 ⁺ 10.2
56 ^b	AGN	206.86557	-30.418478	78.6 ⁺ 2.6	88.4 ⁺ 2.9	83.4 ⁺ 10.9	208.0 ⁺ 9.2
57 ^b	E*	206.86574	-30.367851	173.0 ⁺ 3.5	116.0 ⁺ 3.4	73.0 ⁺ 15.2	58.6 ⁺ 10.2
58 ^b	AGN?	206.86612	-30.414799	14.6 ⁺ 2.6	19.4 ⁺ 2.9	17.8 ⁺ 10.8	150.0 ⁺ 9.2
59 ^b	SF	206.87124	-30.476743	236.0 ⁺ 3.5	156.0 ⁺ 3.4	252.0 ⁺ 15.2	944.0 ⁺ 10.2

TABLE 4
- CONT.

Object ^a	RA (J2000) (^o)	Dec (J2000) (^o)	F _{3.6μm} (μ Jy)	F _{4.5μm} (μ Jy)	F _{5.8μm} (μ Jy)	F _{8.0μm} (μ Jy)		
60 ^b	3 -	E*	206.87193	-30.404070	809.0 ⁺ _{3.5}	480.0 ⁺ _{3.4}	293.0 ⁺ _{15.2}	222.0 ⁺ _{10.3}
61 ^b		S0*	206.87499	-30.370020	407.0 ⁺ _{3.5}	306.0 ⁺ _{3.4}	258.0 ⁺ _{15.2}	221.0 ⁺ _{10.3}
62 ^b		N	206.87787	-30.404201	95.5 ⁺ _{2.6}	86.7 ⁺ _{2.9}	42.1 ⁺ _{10.9}	124.0 ⁺ _{9.2}
63 ^b		N	206.87844	-30.455269	80.0 ⁺ _{2.6}	68.9 ⁺ _{2.9}	<16.8	162.0 ⁺ _{9.3}
64 ^b		SF	206.88901	-30.390435	133.0 ⁺ _{3.5}	117.0 ⁺ _{3.4}	96.0 ⁺ _{15.2}	284.0 ⁺ _{10.3}
65 ^b		E*	206.89271	-30.364745	923.0 ⁺ _{3.5}	650.0 ⁺ _{3.4}	404.0 ⁺ _{15.2}	261.0 ⁺ _{10.3}
66 ^b		SF	206.89412	-30.467691	69.3 ⁺ _{3.2}	64.5 ⁺ _{3.3}	31.1 ⁺ _{14.9}	135.0 ⁺ _{10.2}
67 ^b			206.89467	-30.431946	119.0 ⁺ _{3.3}	82.9 ⁺ _{3.2}	87.9 ⁺ _{15.2}	111.0 ⁺ _{10.2}
68 ^b		N	206.89631	-30.437985	60.2 ⁺ _{2.6}	53.1 ⁺ _{2.9}	28.5 ⁺ _{10.9}	87.7 ⁺ _{8.8}
69 ^b		E*	206.89914	-30.395302	201.0 ⁺ _{3.5}	133.0 ⁺ _{3.3}	102.0 ⁺ _{15.2}	54.6 ⁺ _{10.3}
70 ^b			206.90090	-30.367889	241.0 ⁺ _{3.5}	158.0 ⁺ _{3.3}	124.0 ⁺ _{15.2}	175.0 ⁺ _{10.2}
71 ^b		N	206.90105	-30.460684	243.0 ⁺ _{3.5}	151.0 ⁺ _{3.4}	75.6 ⁺ _{15.2}	131.0 ⁺ _{10.2}
72 ^b			206.90456	-30.421585	37.8 ⁺ _{3.5}	49.9 ⁺ _{3.3}	36.5 ⁺ _{14.4}	114.0 ⁺ _{10.2}
73 ^b		AGN	206.91035	-30.448771	45.7 ⁺ _{3.5}	43.5 ⁺ _{3.4}	82.6 ⁺ _{15.2}	94.7 ⁺ _{10.2}
74 ^b			206.91079	-30.450288	22.7 ⁺ _{3.2}	65.0 ⁺ _{3.3}	<41.2	73.5 ⁺ _{9.7}
75 ^b		N	206.91286	-30.439546	142.0 ⁺ _{3.5}	129.0 ⁺ _{3.4}	36.4 ⁺ _{15.2}	204.0 ⁺ _{10.0}

^aSecond column is the L79/M97 and DM98 naming convention. Third column is the classification from the SED match in SS3.5, T: candidate TDG, SF: reasonable fit to TDG-N, star-forming region, N: “notched” SED but poor match to TDG-N, E: elliptical, E*: elliptical/foreground star, S0 : S0, S0* : S0/foreground star, AGN :AGN, AGN? : not a simple power-law

^bSource is outside HI ring.

^cGalaxy 435 (Richter 1984, M97).

^d16 pixel diameter aperture.

^eTDG-N. Source K09.09 (Pena, Ruiz & Maza 1991)

^fTDG-S., the tail is source G in L79

^gMag. auto flux density as source is extended beyond 16 pixel diam. aperture. Note the aperture correction for an infinitely extended source has not been applied. The correction factors listed in the SOM are 0.94, 0.94, 0.63, 0.69 at [3.6] , [4.5] , [5.8] , [8.0] , respectively.

^hSeashell.

ⁱNGC 5291.

FIG. 1.— The IRAC “non-stellar” image of the NGC 5291 system created by subtracting stellar light from the 8.0 μm image (see text). This emission is most likely dominated by strong 7.7 μm and 8.6 μm PAH bands. Arrows identify sources listed in Table 4. For example, # 26 & 33 are TDG-N and TDG-S, respectively. NGC 5291 is # 44 and the Seashell is #35. The contours show the distribution of HI ($\Sigma_{\text{HI}} = 1, 3, 5, 7 \text{ \& } 9 M_{\odot} \text{ pc}^{-2}$) created by reprocessing the VLA DnC archive data ($\theta_{\text{FWHM}} = 50''$). Original VLA data published by Malphrus et al. (1997).

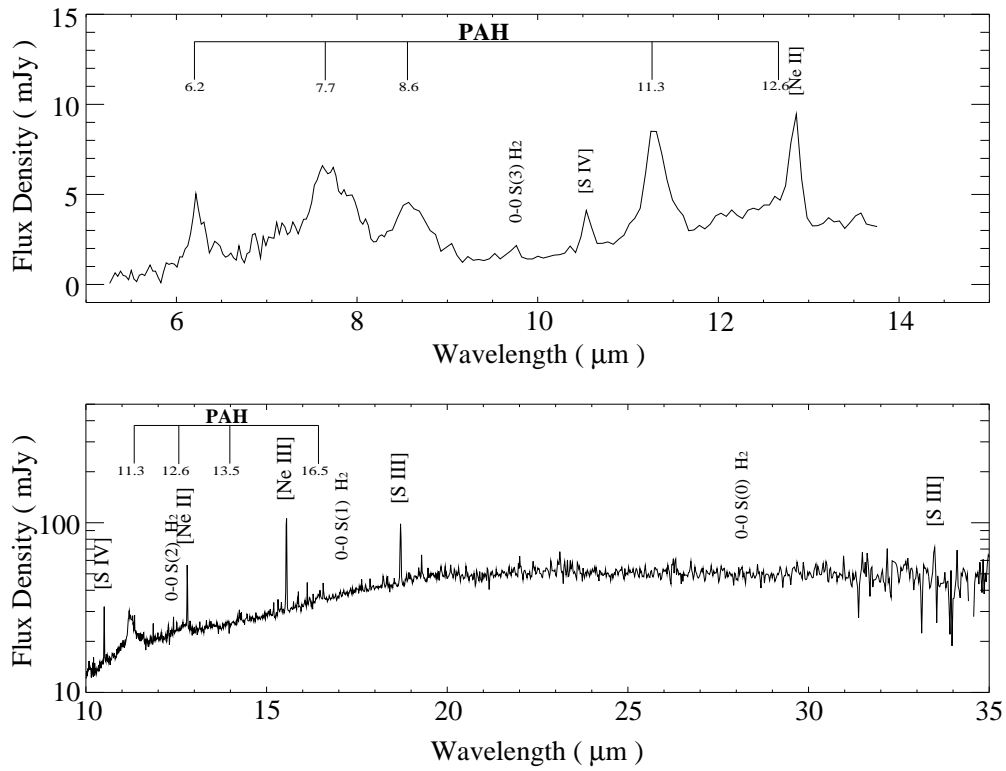


FIG. 2.— Spitzer IRS spectra of TDG-N. (Top) IRS-SL spectrum showing strong PAH features and 0-0 S(3) 9.7 μm molecular Hydrogen. (Bottom). Combined IRS-SH & IRS-LH spectrum showing PAHs and fine structure lines. The flattening of the continuum emission beyond $\lambda > 20 \mu\text{m}$ signifies the absence of a dominant cool 40 K dust component.

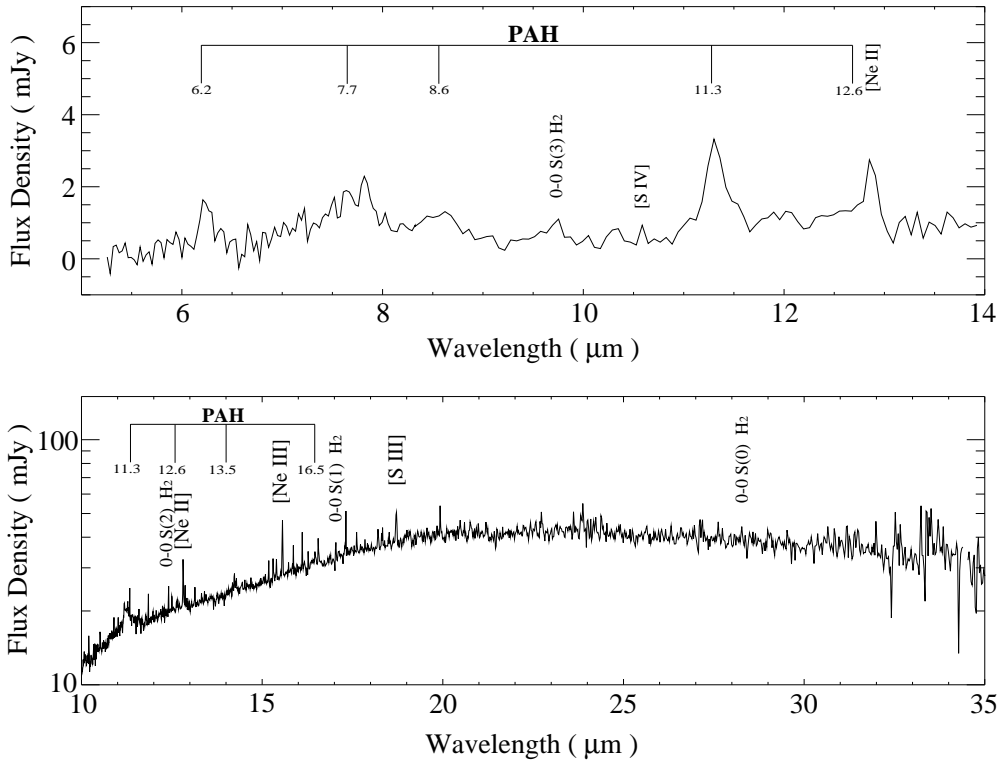


FIG. 3.— Spitzer IRS spectra of TDG-S. (Top) IRS-SL spectrum showing strong PAH features and 0-0 S(3) 9.7 μm molecular Hydrogen. (Bottom). Combined IRS-SH & IRS-LH spectrum showing PAHs and fine structure lines. The flattening of the continuum emission beyond $\lambda > 20 \mu\text{m}$ signifies the absence of a dominant cool 40 K dust component.

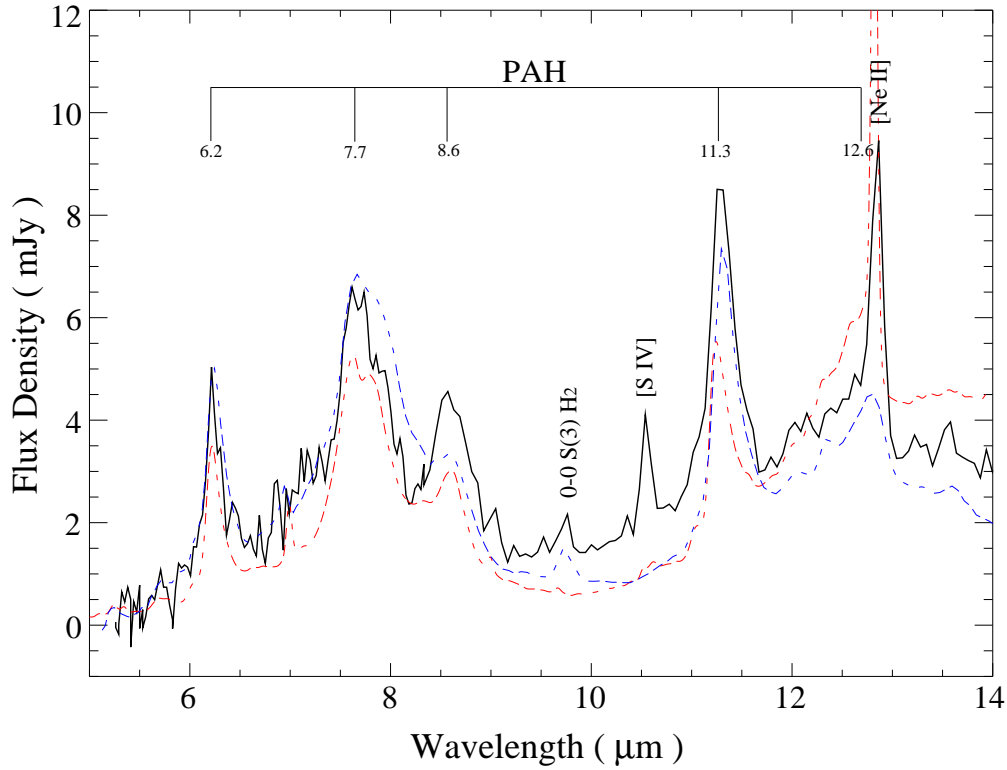


FIG. 4.— A comparison between the IRS Short-Low spectrum of TDG-N (thick black line), the ISO-SWS spectrum of the starburst galaxy M 82 dash line (dashed red-line electronic edition) from Lutz et al. (1998) after smoothing to the IRS Short-Low resolution and normalized to $7 \mu\text{m}$, and an IRS Short-Low spectrum of the reflection nebula NGC 7023 normalized to $7 \mu\text{m}$ thin line (dashed blue-line electronic edition) from Werner et al. 2004b, showing the remarkable similarity in shape. Note the $[\text{Ne II}]$ $12.81 \mu\text{m}$ line is blended with the $12.6 \mu\text{m}$ PAH.

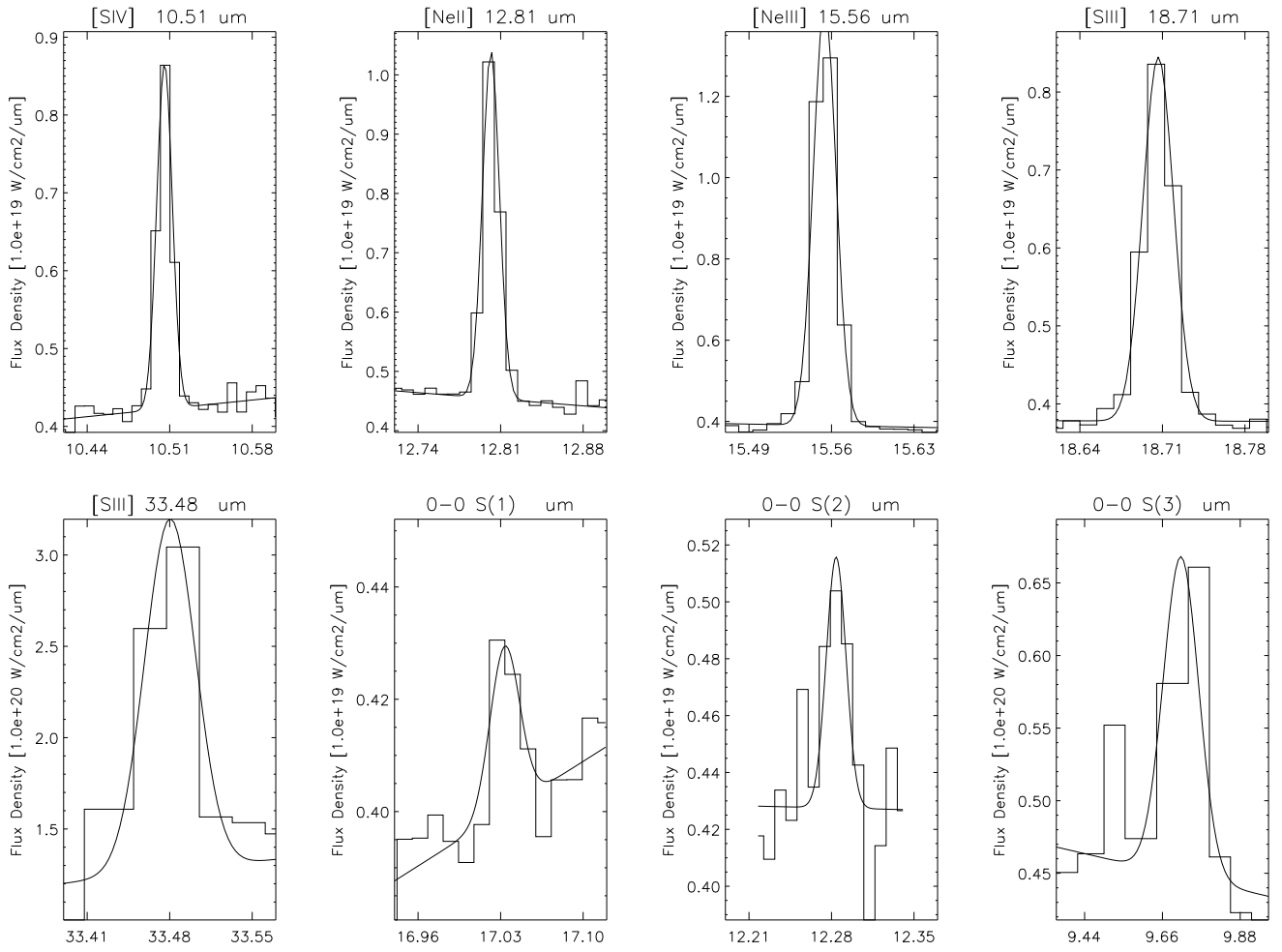


FIG. 5.— Spitzer spectra of emission lines detected in TDG-N (histogram). The lines were fit with a Gaussian profile combined with a first order polynomial fit to the continuum (solid line). The lines are from IRS-SH/LH, except 0-0 S(3), which was observed with IRS-SL.

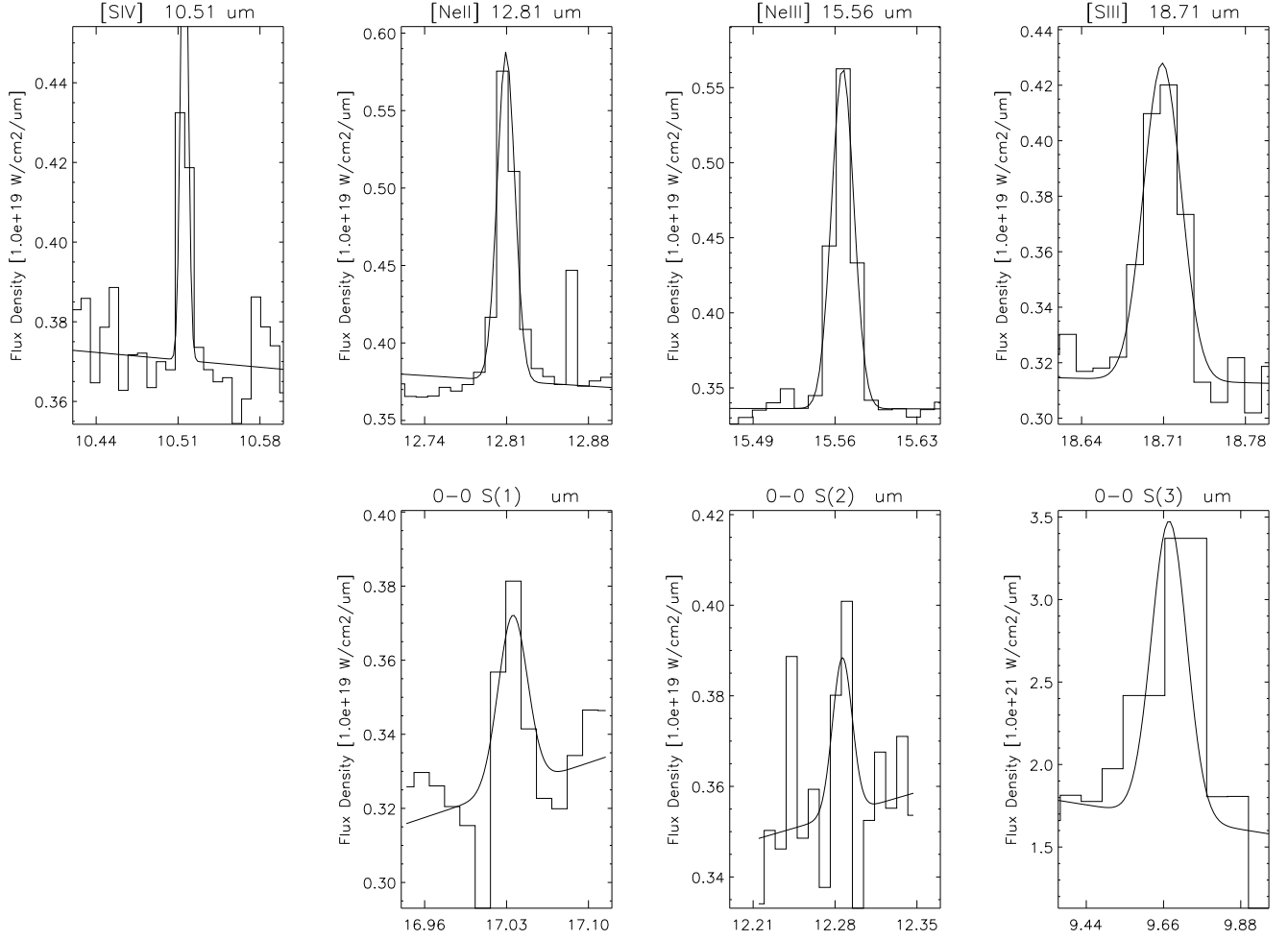


FIG. 6.— Spitzer IRS spectra of emission lines detected in TDG-S (histogram). The lines were fit with a Gaussian profile combined with a first order polynomial fit to the continuum (solid line). The lines are from IRS-SH/LH, except 0-0 S(3), which was observed with IRS-SL. All lines were detected in both nod positions except for the 0-0 S (2) line.

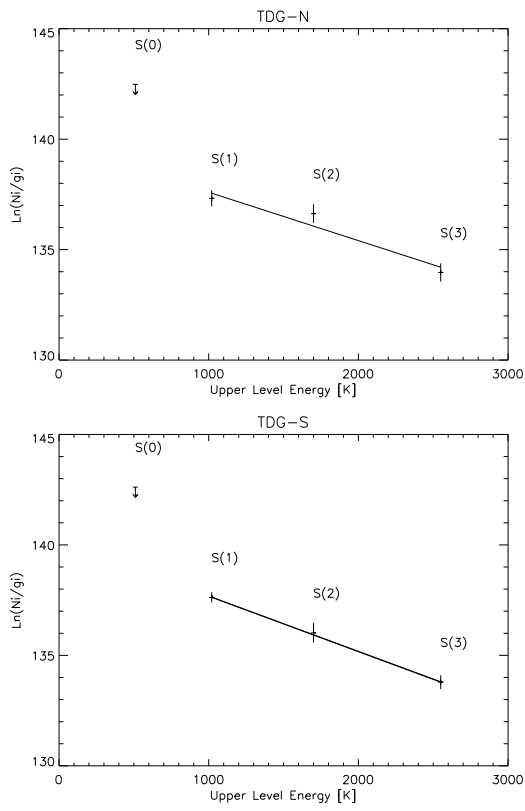


FIG. 7.— Excitation Diagrams for TDG-N (left) and TDG-S (right). The absolute value of the reciprocal of the slope is the excitation temperature.

FIG. 8.— IRAC false color image of the NGC 5291 system, defined by $3.6 \mu\text{m}$ (blue), $4.5 \mu\text{m}$ (green), $5.8 \mu\text{m}$ (orange) and $8.0 \mu\text{m}$ (red). Sources dominated by starlight (e.g. NGC 5291 & ‘Seashell’) are blue in color while objects with strong PAH emission, including TDGs and the flocculent spiral galaxy (#5 in Table 4), are red in color.

FIG. 9.— (Top-left), IRAC 3.6 μm image of the NGC 5291 system. A linear stretch between -0.04 and 1.6 MJy sr^{-1} is used. The scalebar represents $1'$, i.e., a linear scale of 18 kpc . (Top-right), IRAC 4.5 μm image. A linear stretch between -0.05 and 1.2 MJy sr^{-1} is used. (Bottom-left), IRAC 5.8 μm image. A linear stretch between -0.13 and 0.71 MJy sr^{-1} is used. (Bottom-right), IRAC 8.0 μm image. A linear stretch between -0.10 and 0.72 MJy sr^{-1} is used.

Fig. 9 — cont.

Fig. 9 — cont.

Fig. 9 — cont.

FIG. 10.— Close-ups of TDG-N (# 26), TDG-S (# 33) and candidate TDGs associated with NGC 5291 showing emission at $3.6 \mu\text{m}$ (top-row) and “non-stellar” emission from PAHs (bottom row). The vertical bar represents $30''$, i.e., a linear scale of 9 kpc.

FIG. 11.— IRAC images of NGC 5291 and the “Seashell” galaxy, showing (top-left) $3.6\ \mu\text{m}$ emission, (top-right) $3.6\ \mu\text{m}$ emission with surface brightness contours, (bottom-left) “non-stellar” emission, and (bottom-right) “non-stellar” emission after smoothing with a $5''$ Gaussian kernel. The images are displayed with a logarithmic stretch between 0.1 and $1.0\ \text{MJy sr}^{-1}$, and the contours are equally spaced in log-space between 0.3 and $30.0\ \text{MJy sr}^{-1}$.

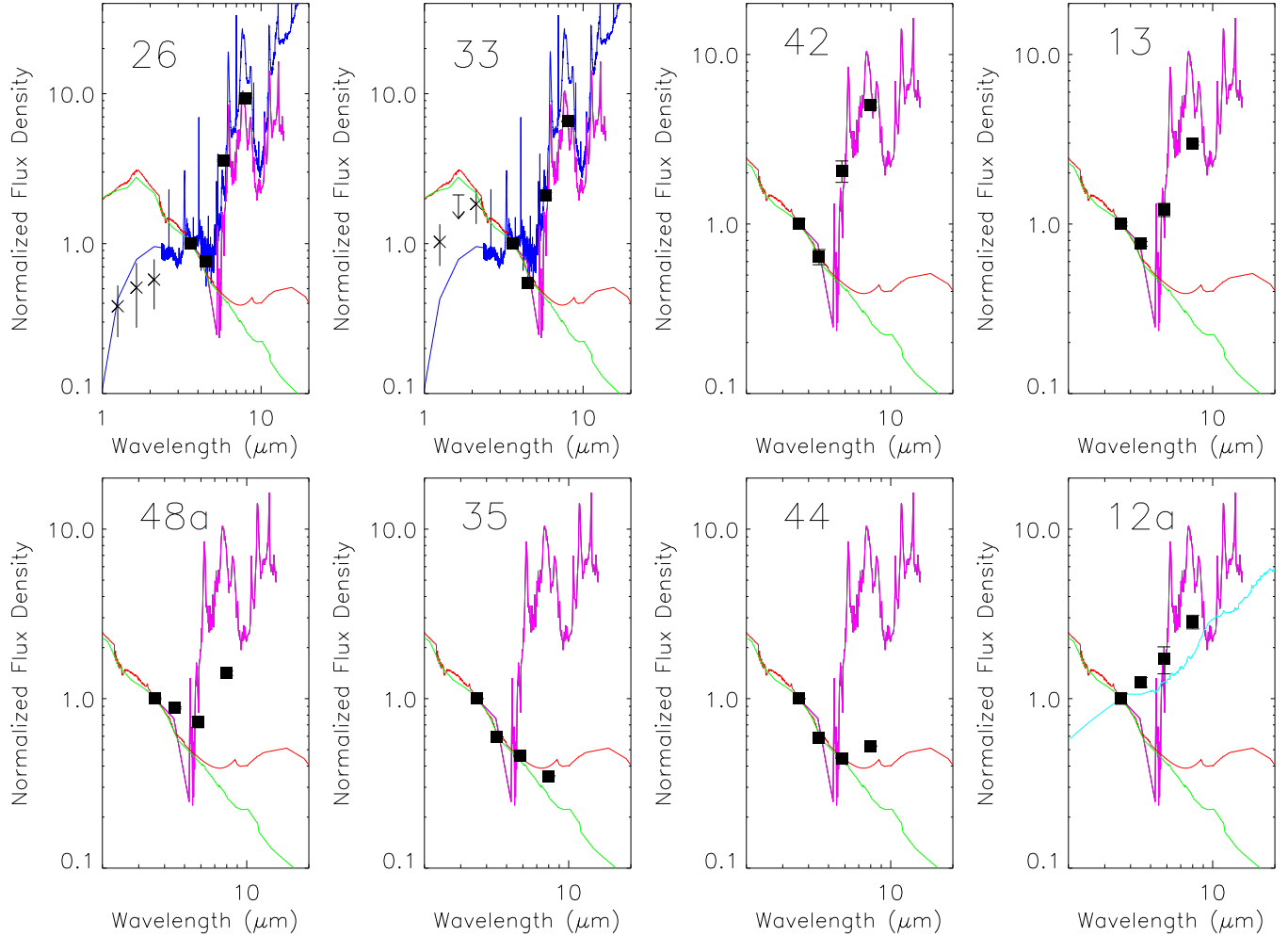


FIG. 12.— Example IRAC Spectral Energy Distributions (SEDs) overlaid with a series of template galaxies: TDG-N the solid line (colored pink in electronic edition), Elliptical the dot-dash line (Silva et al. 1998, colored green in electronic edition), S0 the dot-dot-dot-dash line (Devriendt, Guiderdoni & Sadat, R. 1999, colored red in electronic edition), M 82 nuclear region the dotted line (Lutz et al 1998, colored dark blue in electronic edition) and an I Zw 1 the dash-line (Weedman et al. 2005, colored light blue in electronic edition). Sources with the suffix ‘a’ are outside the projected HI ring. TDG-N is #26, TDG-S is #33. #42 is an example of a good match to TDG-N i.e., a candidate TDG, #13 is a reasonable match to TDG-N and characterized as a star forming region, #48a is a “notched” SED indicating star formation, the Seashell (#35) matches both the elliptical and S0 templates, NGC 5291 (#44) matches the S0 template and #12a is a power-law, characteristic of an AGN.

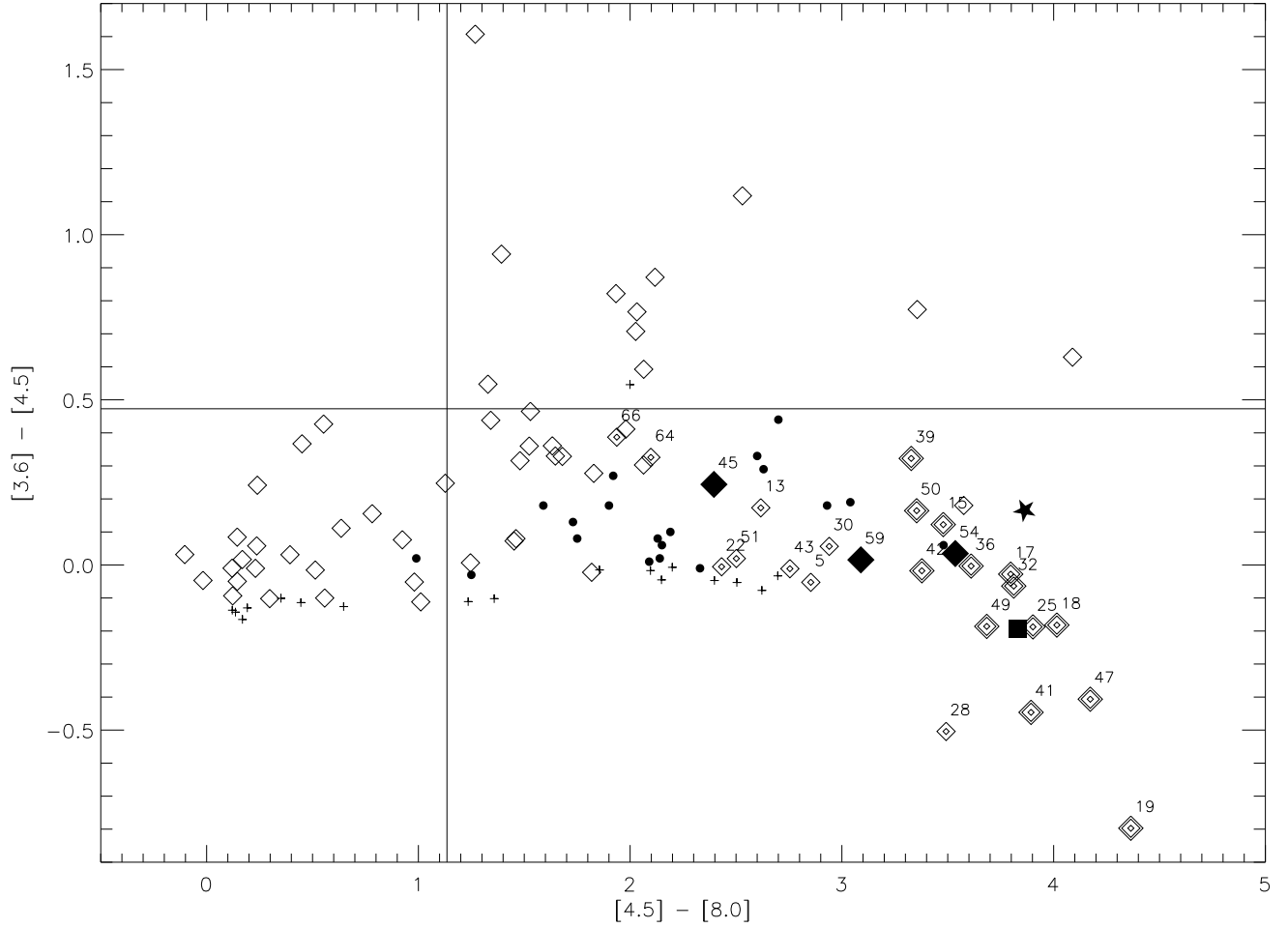


FIG. 13.— $[4.5] - [8.0]$ versus $[3.6] - [4.5]$ color – color plot. The horizontal and vertical lines mark the color zero-points. A source with a flat SED would lie on the crossing point of these two lines. Sources in the lower left quadrant have falling SEDs typical of NGC 5291 and the Seashell, i.e., E and S0 galaxies. AGN like sources, with rising SEDs, are located in the upper right quadrant. The lower right quadrant contains sources with active star formation. TDG-N and TDG-S are shown as a small solid star and square, respectively. The diamonds represent the remaining sources from Table 4. In particular, framed-diamonds denote the 13 candidate TDGs. Sources located within the HI ring that are a reasonable match to TDG-N, but with weaker PAH emission, are shown as double-diamonds. Sources outside the HI ring with TDG-like SEDs are shown as solid diamonds. Source identification numbers are from Table 4. For comparison the Pahre et al. (2004) galaxy sample are shown as crosses and the Rosenberg et al. (2005) BCDs are shown as solid circles. The TDGs and candidate TDGs all show significantly enhanced non-stellar emission, most likely due to PAHs, relative to normal spirals and even BCD galaxies.

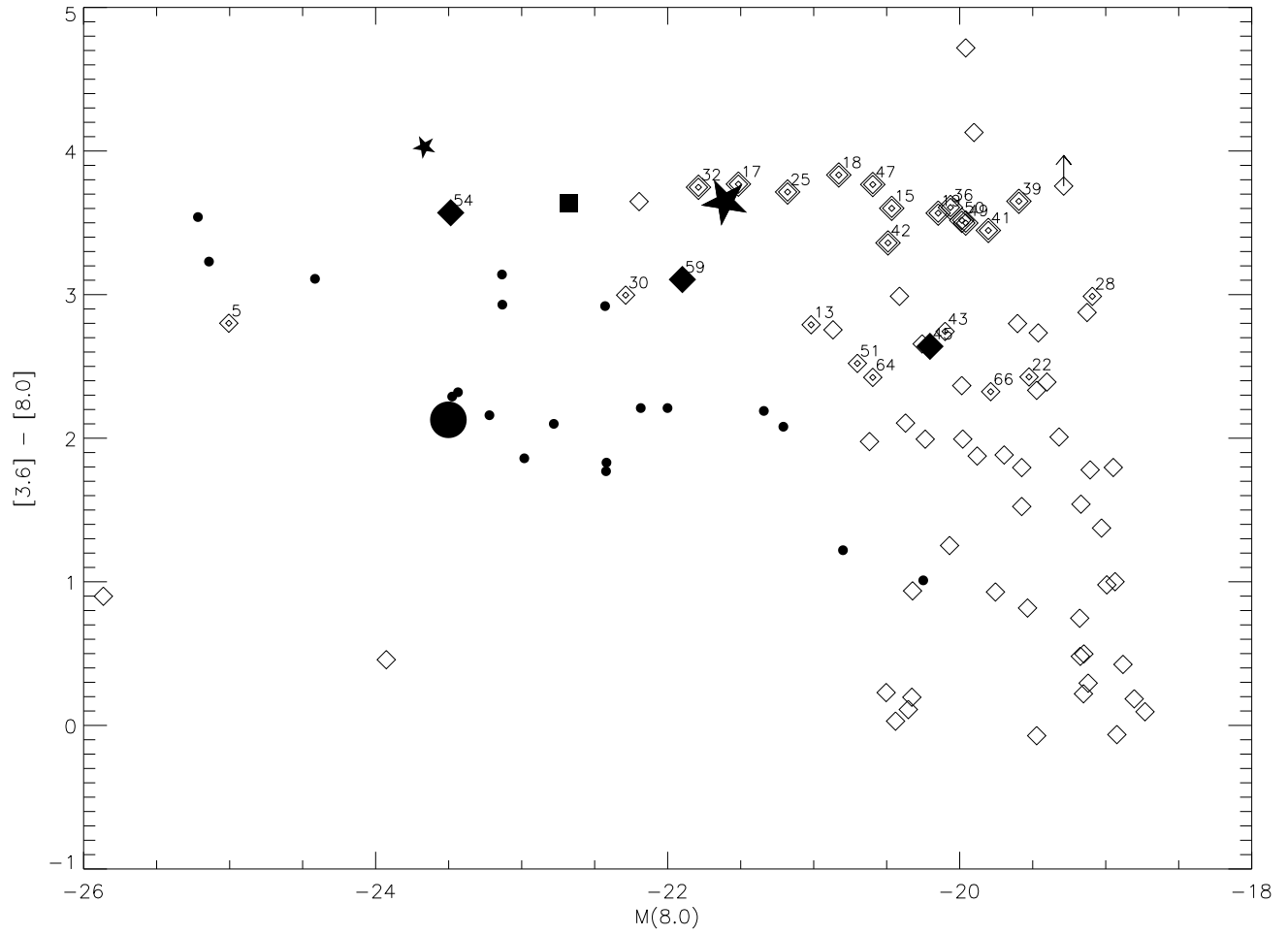


FIG. 14.— $[3.6] - [8.0]$ color versus $[8.0]$ absolute magnitude. See the caption to Figure 13 for symbol definitions. The average positions of the TDG/TDG-candidate and BCD samples are indicated by the large star and circle, respectively. The candidate TDGs occupy a distinct region, being on average ~ 2.2 magnitudes redder in $[3.6] - [8.0]$ color and 2.2 magnitudes fainter at $8 \mu\text{m}$ than the Rosenberg et al. (2005) BCD sample.

This figure "f1.jpeg" is available in "jpeg" format from:

<http://arxiv.org/ps/astro-ph/0511422v1>

This figure "f8.jpeg" is available in "jpeg" format from:

<http://arxiv.org/ps/astro-ph/0511422v1>

This figure "f9a.jpeg" is available in "jpeg" format from:

<http://arxiv.org/ps/astro-ph/0511422v1>

This figure "f9b.jpeg" is available in "jpeg" format from:

<http://arxiv.org/ps/astro-ph/0511422v1>

This figure "f9c.jpeg" is available in "jpeg" format from:

<http://arxiv.org/ps/astro-ph/0511422v1>

This figure "f9d.jpeg" is available in "jpeg" format from:

<http://arxiv.org/ps/astro-ph/0511422v1>

This figure "f10.jpeg" is available in "jpeg" format from:

<http://arxiv.org/ps/astro-ph/0511422v1>

This figure "f11.jpeg" is available in "jpeg" format from:

<http://arxiv.org/ps/astro-ph/0511422v1>